DGK Veröffentlichungen der DGK

Ausschuss Geodäsie der Bayerischen Akademie der Wissenschaften

Reihe C | Dissertationen | Heft Nr. 902

Lasse Klingbeil

Georeferencing of Mobile Mapping Data

München 2023

Bayerische Akademie der Wissenschaften

ISSN 0065-5325 ISBN 978-3-7696-5314-4

Diese Arbeit ist gleichzeitig veröffentlicht in:
bonndoc – Publikationsserver der Rheinischen Friedrich-Wilhelms-Universität Bonn
https://bonndoc.ulb.uni-bonn.de/xmlui/handle/20.500.11811/10926, Bonn 2023

DGK Veröffentlichungen der DGK

Ausschuss Geodäsie der Bayerischen Akademie der Wissenschaften

Reihe C Dissertationen Heft Nr. 902

Georeferencing of Mobile Mapping Data

An der Landwirtschaftlichen Fakultät
der Rheinischen Friedrich-Wilhelms-Universität Bonn
Institut für Geodäsie und Geoinformation
eingereichte kumulative Habilitationsschrift
zur Erlangung der Lehrbefähigung im Fachgebiet Ingenieurgeodäsie

von

Dr. rer. nat. Lasse Klingbeil

Geboren am 13.01.1975 in Siegburg, Deutschland

München 2023

Bayerische Akademie der Wissenschaften

ISSN 0065-5325 ISBN 978-3-7696-5314-4

Diese Arbeit ist gleichzeitig veröffentlicht in:

bonndoc – Publikationsserver der Rheinischen Friedrich-Wilhelms-Universität Bonn
https://bonndoc.ulb.uni-bonn.de/xmlui/handle/20.500.11811/10926, Bonn 2023

Adresse der DGK:

Ausschuss Geodäsie der Bayerischen Akademie der Wissenschaften (DGK)

Alfons-Goppel-Straße 11 ● D – 80 539 München

Telefon +49 – 331 – 288 1685 ● E-Mail post@dgk.badw.de

http://www.dgk.badw.de

Erstgutachter: Prof. Dr.-Ing. Heiner Kuhlmann (Rheinische Friedrich-Wilhelms-Universität Bonn)

Zweitgutachter: Prof. Dr. Cyrill Stachniss (Rheinische Friedrich-Wilhelms-Universität Bonn)

Tag der Habilitation: 18. Januar 2023

ISSN 0065-5325 ISBN 978-3-7696-5314-4

Abstract

One of the main tasks in Engineering Geodesy is the measurement and monitoring of geometry related phenomena on local or regional scales. Examples are the generation of high-resolution 3D city models, as they are needed for autonomous driving, and the monitoring of artificial or natural objects, such as bridges, glaciers or sliding slopes. In the last decade, these tasks have been more and more realized using mobile sensor platforms, such as robots, cars, or Unmanned Aerial Vehicles (UAVs). The platforms are equipped with laser scanners and cameras and collect data while moving through the environment. In this way, it is possible to perform the task of mapping an area of interest with a much higher density and efficiency.

A crucial part of this mobile mapping process is the georeferencing of the locally acquired sensor data, registering those data in a globally defined coordinate system. For this, it is necessary to know the vehicle's trajectory during the measurement process. This thesis introduces several contributions to the general field of trajectory estimation of moving platforms, including better sensor configurations, new calibration procedures and improved processing algorithms. Another set of contributions describes the development, calibration and evaluation of some specific mobile mapping systems. These are airborne and ground-based systems, with applications ranging from general surveying and deformation analysis to agriculture.

Contents

Publications

Peer-Reviewed after Dissertation, Used as Basis for this Cumulative Thesis

The full text of all publications can be found on the USB stick.

Book Chapters

[B1] **Klingbeil**, L. (**2022**). Georeferencing UAV measurements. In Eltner, A., Hoffmeister, D., Kaiser, A., Karrasch, P., Klingbeil, L., Stöcker, C., and Rovere, A., editors, *UAVs for the Environmental Sciences*, pages 87–108. wbg Academic Darmstadt

[B2] Kuhlmann, H. and **Klingbeil**, L. (**2015**). Mobile Multisensorsysteme. In *Handbuch der Geodäsie*, pages 1–36. Springer Berlin Heidelberg

Journal Articles

[J1] Zabawa, L., Kicherer, A., **Klingbeil**, L., Töpfer, R., Roscher, R., and Kuhlmann, H. (**2022**). Image-based analysis of yield parameters in viticulture. *Biosystems Engineering*, 218:94–109

[J2] Dreier, A., Janßen, J., Kuhlmann, H., and **Klingbeil**, L. (**2021**). Quality analysis of direct georeferencing in aspects of absolute accuracy and precision for a UAV-based laser scanning system. *Remote Sensing*, 13(18):3564

[J3] Lucks, L., **Klingbeil**, L., Plümer, L., and Dehbi, Y. (**2021**). Improving trajectory estimation using 3D city models and kinematic point clouds. *Transactions in GIS*, 25(1):238–260

[J4] Honecker, A., Schumann, H., Becirevic, D., **Klingbeil**, L., Volland, K., Forberig, S., Jansen, M., Paulsen, H., Kuhlmann, H., and Léon, J. (**2020**). Plant, space and time - linked together in an integrative and scalable data management system for phenomic approaches in agronomic field trials. *Plant Methods*, 16(1):55

[J5] Zabawa, L., Kicherer, A., **Klingbeil**, L., Töpfer, R., Kuhlmann, H., and Roscher, R. (**2020**). Counting of grapevine berries in images via semantic segmentation using convolutional neural networks. *ISPRS Journal of Photogrammetry and Remote Sensing*, 164:73–83

[J6] Eichel, J., Draebing, D., Kattenborn, T., Senn, J. A., **Klingbeil**, L., Wieland, M., and Heinz, E. (**2020**). Unmanned aerial vehicle-based mapping of turf-banked solifluction

lobe movement and its relation to material , geomorphometric , thermal and vegetation properties. *Permafrost and Periglacial Processes*, 31(1):97–109

[J7] Heinz, E., Holst, C., Kuhlmann, H., and **Klingbeil**, L. (**2020**). Design and evaluation of a permanently installed plane-based calibration field for mobile laser scanning systems. *Remote Sensing*, 12(3):555

[J8] Zimmermann, F., Schmitz, B., **Klingbeil**, L., and Kuhlmann, H. (**2019**). GPS multipath analysis using fresnel zones. *Sensors*, 19(1):25

[J9] Wilke, N., Siegmann, B., **Klingbeil**, L., Burkart, A., Kraska, T., Muller, O., van Doorn, A., Heinemann, S., and Rascher, U. (**2019**). Quantifying lodging percentage and lodging severity using a UAV-based canopy height model combined with an objective threshold approach. *Remote Sensing*, 11(5):515

[J10] Heinz, E., Eling, C., **Klingbeil**, L., and Kuhlmann, H. (**2019**). On the applicability of a scan-based mobile mapping system for monitoring the planarity and subsidence of road surfaces - pilot study on the A44n motorway in germany. *Journal of Applied Geodesy*, 14(1):39–54

[J11] Zimmermann, F., Holst, C., **Klingbeil**, L., and Kuhlmann, H. (**2018**). Accurate georeferencing of TLS point clouds with short GNSS observation durations even under challenging measurement conditions. *Journal of Applied Geodesy*, 12(4):289–301

[J12] Kicherer, A., Herzog, K., Bendel, N., Klück, H. C., Backhaus, A., Wieland, M., Rose, J. C., **Klingbeil**, L., Läbe, T., Hohl, C., Petry, W., Kuhlmann, H., Seiffert, U., and Töpfer, R. (**2017**). Phenoliner: A new field phenotyping platform for grapevine research. *Sensors*, 17(7):1625

[J13] Eichel, J., Draebing, D., **Klingbeil**, L., Wieland, M., Eling, C., Schmidtlein, S., Kuhlmann, H., and Dikau, R. (**2017**). Solifluction meets vegetation: the role of biogeomorphic feedbacks for turf-banked solifluction lobe development. *Earth Surface Processes and Landforms*, 42(11):1623–1635

[J14] **Klingbeil**, L., Eling, C., Heinz, E., Wieland, M., and Kuhlmann, H. (**2017**). Direct georeferencing for portable mapping systems: In the air and on the ground. *Journal of Surveying Engineering*, 143(4):04017010

[J15] Rose, J. C., Kicherer, A., Wieland, M., **Klingbeil**, L., Töpfer, R., and Kuhlmann, H. (**2016**). Towards automated large-scale 3D phenotyping of vineyards under field conditions. *Sensors*, 16(12):2136

[J16] Heinz, E., Eling, C., Wieland, M., **Klingbeil**, L., and Kuhlmann, H. (**2015**). Development, calibration and evaluation of a portable and direct georeferenced laser scanning system for kinematic 3D mapping. *Journal of Applied Geodesy*, 9(4):227–243

[J17] Eling, C., **Klingbeil**, L., and Kuhlmann, H. (**2015**a). Real-time single-frequency GPS / MEMS - IMU attitude determination of lightweight UAVs. *Sensors*, 15(10):26212–26235

[J18] **Klingbeil**, L., Eling, C., Zimmermann, F., and Kuhlmann, H. (**2014**a). Magnetic field sensor calibration for attitude determination. *Journal of Applied Geodesy*, 8(2):97–108

[J19] Schopp, P., Graf, H., Maurer, M., Romanovas, M., **Klingbeil**, L., and Manoli, Y. (**2014**). Observing relative motion with three accelerometer triads. *IEEE Transactions on Instrumentation and Measurement*, 63(12):3137–3151

[J20] Eling, C., **Klingbeil**, L., Wieland, M., and Kuhlmann, H. (**2014**). Direct georeferencing of micro aerial vehicles - system design, system calibration and first evaluation tests. *Photogrammetrie - Fernerkundung - Geoinformation*, 2014(4):227–237

[J21] Schopp, P., **Klingbeil**, L., Peters, C., and Manoli, Y. (**2010**). Design, geometry evaluation, and calibration of a ggyroscope-free inertial measurement unit. *Sensors and Actuators A: Physical*, 162(2):379–387

[J22] Wark, T., Corke, P., Sikka, P., **Klingbeil**, L., Ying, G., Crossman, C., Valencia, P., Swain, D., and Bishop-Hurley, G. (**2007**). Transforming agriculture through pervasive wireless sensor networks. *IEEE Pervasive Computing*, 6(2):50–57

Conference Papers

[C1] **Klingbeil**, L., Heinz, E., Wieland, M., Eichel, J., Laebe, T., and Kuhlmann, H. (**2019**). On the UAV-based analysis of slow geomorphological processes: A case study at a solifluction lobe in the turtmann valley. In *2019 Joint International Symposium on Deformation Monitoring (JISDM), Athens, Greece*

[C2] Becirevic, D., **Klingbeil**, L., Honecker, A., Schumann, H., Rascher, U., Léon, J., and Kuhlmann, H. (**2019**). On the derivation of crop heights from multitemporal UAV-based imagery. *ISPRS Annals of the Photogrammetry, Remote Sensing and Spatial Information Sciences*, IV-2/W5(2/W5):95–102

[C3] Zabawa, L., Kicherer, A., **Klingbeil**, L., Milioto, A., Töpfer, R., Kuhlmann, H., and Roscher, R. (**2019**). Detection of single grapevine berries in images using fully convolutional neural networks. In *2019 IEEE/CVF Conference on Computer Vision and Pattern Recognition Workshops (CVPRW)*, pages 2571–2579. IEEE

[C4] Heinz, E., Eling, C., Wieland, M., **Klingbeil**, L., and Kuhlmann, H. (**2017**). Analysis of different reference plane setups for the calibration of a mobile laser scanning system. In Lienhart, W., editor, *Ingenieurvermessung 17, Beiträge zum 18. Internationalen Ingenieurvermessungskurs, Graz, Austria*, pages 1–14. Wichmann Verlag

[C5] Holst, C., **Klingbeil**, L., Esser, F., and Kuhlmann, H. (**2017**). Using point cloud comparisons for revealing deformations of natural and artificial objects. In *2017 International Conference on Engineering Surveying (INGEO)*, pages 265–274

[C6] Zimmermann, F., Eling, C., **Klingbeil**, L., and Kuhlmann, H. (**2017**). Precise positioning of UAVs - dealing with challenging RTK-GPS measurement conditions during automated UAV flights. *ISPRS Annals of the Photogrammetry, Remote Sensing and Spatial Information Sciences*, 4:95–102

[C7] Schneider, J., Eling, C., **Klingbeil**, L., Kuhlmann, H., Förstner, W., and Stachniss, C. (**2016**). Fast and effective online pose estimation and mapping for UAVs. In *2016 IEEE International Conference on Robotics and Automation (ICRA)*. IEEE

[C8] Eling, C., **Klingbeil**, L., Wieland, M., and Kuhlmann, H. (**2016**). Towards deformation monitoring with UAV- based mobile mapping systems. In *2016 Joint International Symposium on Deformation Monitoring (JISDM), TU Wien, Vienna*

[C9] Eling, C., Wieland, M., Hess, C., **Klingbeil**, L., and Kuhlmann, H. (**2015**b). Development and evaluation of a UAV-based mapping system for remote sensing and surveying applications. *The International Archives of the Photogrammetry, Remote Sensing and Spatial Information Sciences*, XL-1/W4(1W4):233–239

[C10] **Klingbeil**, L., Nieuwenhuisen, M., Schneider, J., Eling, C., Droeschel, D., Holz, D., Läbe, T., Förstner, W., Behnke, S., and Kuhlmann, H. (**2014**b). Towards autonomous navigation of a UAV-based mobile mapping system. In *2014 International Conference on Machine Control and Guidance (MCG)*, pages 136–147

[C11] Romanovas, M., Goridko, V., **Klingbeil**, L., Bourouah, M., Al-Jawad, A., Traechtler, M., and Manoli, Y. (**2013**). Pedestrian indoor localization using foot mounted inertial sensors in combination with a magnetometer, a barometer and RFID. In *Lecture Notes in Geoinformation and Cartography*, pages 151–172. Springer Berlin Heidelberg

[C12] **Klingbeil**, L., Romanovas, M., Schneider, P., Traechtler, M., and Manoli, Y. (**2010**). A modular and mobile system for indoor localization. In *2010 International Conference on Indoor Positioning and Indoor Navigation (IPIN)*. IEEE

[C13] Schopp, P., **Klingbeil**, L., Peters, C., Buhmann, A., and Manoli, Y. (**2009**). Sensor fusion algorithm and calibration for a gyroscope-free IMU. *Procedia Chemistry*, 1(1):1323–1326

[C14] Romanovas, M., **Klingbeil**, L., Trächtler, M., and Manoli, Y. (**2009**). Efficient orientation estimation algorithm for low cost inertial and magnetic sensor systems. In *2009 IEEE/SP 15th Workshop on Statistical Signal Processing*. IEEE

[C15] **Klingbeil**, L. and Wark, T. (**2008**). A wireless sensor network for real-time indoor localisation and motion monitoring. In *2008 International Conference on Information Processing in Sensor Networks (IPSN)*. IEEE

[C16] **Klingbeil**, L., Wark, T., and Bidargaddi, N. (**2007**). Efficient transfer of human motion data over a wireless delay tolerant network. In *2007 3rd International Conference on Intelligent Sensors, Sensor Networks and Information (ISSNIP)*. IEEE

Chapter 1

Introduction

[**B2**] Kuhlmann, H. and **Klingbeil**, L. (**2015**). Mobile Multisensorsysteme. In *Handbuch der Geodäsie*, pages 1–36. Springer Berlin Heidelberg

[**J14**] **Klingbeil**, L., Eling, C., Heinz, E., Wieland, M., and Kuhlmann, H. (**2017**). Direct georeferencing for portable mapping systems: In the air and on the ground. *Journal of Surveying Engineering*, 143(4):04017010

[**B1**] **Klingbeil**, L. (**2022**). Georeferencing UAV measurements. In Eltner, A., Hoffmeister, D., Kaiser, A., Karrasch, P., Klingbeil, L., Stöcker, C., and Rovere, A., editors, *UAVs for the Environmental Sciences*, pages 87–108. wbg Academic Darmstadt

1.1 Mobile Mapping

With mobile mapping systems, it is possible to create maps of the environment with high efficiency. We consider a map a two- or three-dimensional geometric representation of the area of interest, sometimes augmented with additional information, such as colour, temperature, or spectral reflectance. Mobile mapping systems are aerial or ground-based vehicles usually equipped with laser scanners or cameras to map the surrounding space. Although the early aerial surveying planes and remote sensing satellites were not called mobile mapping systems, they can be seen as the predecessors of this modern measurement technology. Nowadays, the platforms move closer to the objects of interest. The sensors have a higher resolution and a higher measurement rate to create maps with higher resolution and accuracy.

The list of applications for mobile mapping systems is long. High-resolution 3D models of whole cities can be used for autonomous driving, planning construction projects, or monitoring the quality of the transportation infrastructure. The systems are also used in many areas of environmental monitoring, such as geomorphology, agriculture and forestry. Depending on the applications and the

used mapping platforms, the derived products differ significantly in their expansion, resolution, accuracy or type of information. In all cases, the georeferencing of the sensor data is the key step in the map-generation process.

1.2 Georeferencing

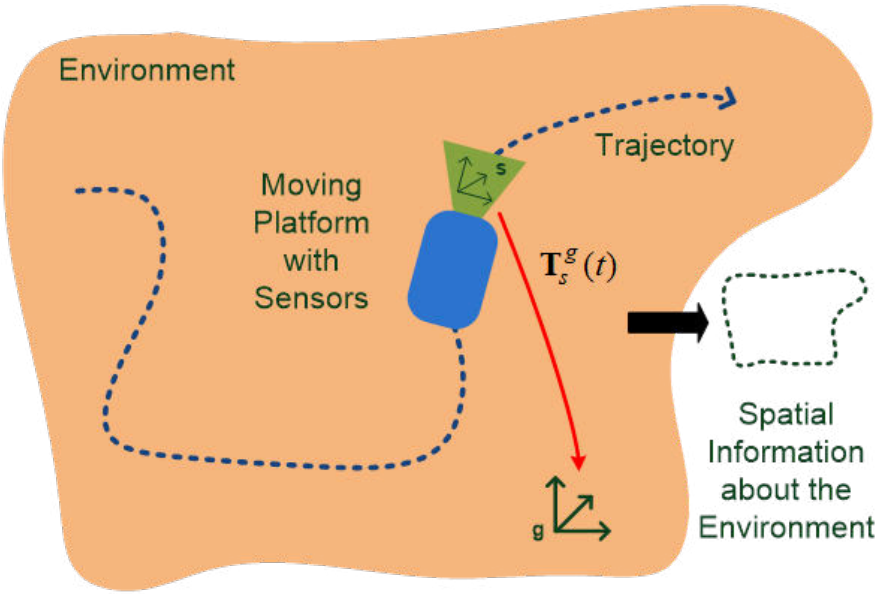

Figure 1.1: Principle of Mobile Mapping and georeferencing.

Fig. 1.1 illustrates the concept of georeferencing of mobile mapping data. The platform with the attached mapping sensor moves through the environment of interest. It collects data about the environment in the form of sensor data, given in the sensor coordinate frame. In order to register these local data in a global coordinate frame, the transformation $\mathbf{T}_s^g(t_k)$ between the sensor frame and the global frame needs to be known for all measurement times t_k. This transformation strongly depends on the platform's trajectory, which is needed in the georeferencing process. We now further explain this process for the examples of mobile laser scanning and image-based mapping.

Mobile Laser Scanning A laser scanner, which is attached to the platform observes an object point (o) in the environment at the time t_k in the local laser scanner coordinate system (s) as $\mathbf{x}_o^s(t_k)$. The process of georeferencing determines the transformation $\mathbf{T}_s^g$, which is necessary to provide the object coordinate $\mathbf{x}_o^g$ in the global coordinate system (g):

$$\mathbf{x}_o^g = \mathbf{T}_s^g(t_k)\mathbf{x}_o^s(t_k). \tag{1.1}$$

$\mathbf{T}$ here describes a rotation and a translation. The coordinate system (b) of the mobile platform can be integrated as well, leading to

$$\mathbf{x}_o^g = \mathbf{T}_b^g(t_k)\mathbf{T}_s^b(t_k)\mathbf{x}_o^s(t_k). \tag{1.2}$$

This equation is called *georeferencing equation*, and the derivation of the series of transformations $\mathbf{T}_b^g(t_k)$ corresponds to the already mentioned trajectory of the platform. The derivation of $\mathbf{T}_s^b(t_k)$ is called *system calibration*. In most cases, the transformation $\mathbf{T}_s^b(t_k)$ can be considered constant over time. However, in the general case, it can also change over time. An overview of the principles of mobile laser scanning is given in [B2]. In Ch. 4 we provide more details on the calibration and application of mobile laser scanning.

Image-Based Mapping The formulation of the georeferencing equation is not as straightforward for the case of systems, where the map is generated from images. The reason is that an image is not a direct 3D measurement of an object point, which only needs to be transformed to the target coordinate system. Instead, it is a measurement of the direction of the point without distance information. Therefore the object point must be reconstructed from multiple observations, usually in an adjustment procedure. We can write that the sensor observation (pixel coordinate) $\mathbf{x}_o^s(t_k)$ of an object or feature $\mathbf{x}_o^g$ in the global coordinate system is a projection $\mathbf{P}_g^s(t_k)$ from the global system (g) to the sensor system (s):

$$\mathbf{x}_o^s(t_k) = \mathbf{P}_g^s(t_k)\mathbf{x}_o^g. \tag{1.3}$$

The projection $\mathbf{P}_g^s$ is a function of the internal camera calibration parameters $\mathbf{C}(t_k)$ and the exterior orientation $\mathbf{T}_s^g(t_k)$, which describes the position and orientation of the camera system (s) with respect to the global system (g).

$$\mathbf{x}_o^s(t_k) = \mathbf{P}_g^s\left(\mathbf{T}_s^g(t_k), \mathbf{C}(t_k)\right)\mathbf{x}_o^g \tag{1.4}$$

The goal of the mapping procedure is to reconstruct a set of multiple object or feature points $\{\mathbf{x}_{o_i}^g\}$ (often called *structure*) from multiple observations $\mathbf{x}_o^s(t_k)$, which have been taken from multiple orientations of the sensor $\mathbf{T}_s^g(t_k)$ (often called *motion*). In the case of given camera orientations, this estimation is called *structure-from-motion*. Also, if the camera orientations are unknown, the structure, the motion and the internal camera calibration parameters can be estimated from multiple observations using a so-called *bundle adjustment*. However, to provide the structure in a global coordinate system, some control information, such as camera positions or object point positions, needs to be known in the global coordinate system. Within this thesis, we will not describe the details of the

underlying photogrammetric algorithms, such as bundle adjustment. However, it should be obvious now that the trajectory $\mathbf{T}_s^g(t_k)$ of the sensor, which again can be separated into the platform trajectory $\mathbf{T}_b^g(t_k)$ and the system calibration $\mathbf{T}_s^b(t_k)$, also plays a significant role in image-based mapping, mainly as an input to the bundle adjustment for georeferencing. An overview of the georeferencing options for UAV data is given in [B1]. In Ch. 5 we provide some examples of image-based mapping.

If the procedure only uses trajectory information $\mathbf{T}_b^g(t_k)$, it is called *direct georeferencing*. In cases, where known objects points $\{\mathbf{x}_{o_i}^g\}$ are used, it is called *indirect georeferencing*. Combinations are called *integrated approaches*. Mostly, mobile laser scanning uses direct referencing, while image-based mapping systems use integrated or indirect approaches.

1.3 Contribution and Structure of the Thesis

The contributions of this thesis are all along the processing chain, which derives useful georeferenced information from laser scanners or cameras mounted on a moving platform. We organized the contributions into five chapters. Chapters 2 and 3 deal with the general task of calculating the platform's trajectory, which is a crucial part of the chain. Chapters 4, 5, and 6 describe the development, calibration, and evaluation of some specific systems, which we used for various applications.

Chapter 2: Inertial Navigation Inertial navigation is a method to derive the trajectory of a platform from inertial sensors and GNSS. It is commonly used to georeference sensor data from mobile mapping systems. This chapter briefly describes the sensors and algorithms behind inertial navigation. Our key contributions in this context are:

1. The development of an inertial measurement unit without a gyroscope, which consists only of multiple distributed accelerometers. With this concept, it is possible to determine all parameters usually derived from an IMU while avoiding the error characteristics that are common for low-cost gyroscopes.

2. A calibration procedure for magnetic field sensors. This procedure does not need reference information and can be easily applied to a specific measurement environment. It calibrates hard and soft-iron effects if the sensor is in a metallic environment and can also be used to calibrate accelerometers.

3. A procedure to characterize the influence of multi-path and non-line of sight effects on the resulting GNSS position measurement. With this, it is

possible to mask certain satellites based on the 3D information about the antenna environment.

4. An efficient Kalman Filter for orientation estimation based on inertial and magnetic sensors, optimized for low-cost sensors and high-dynamic motions.

5. An estimation algorithm to derive the full pose of a UAV in real-time using inertial sensors and two GNSS receivers.

Chapter 3: Localization in GNSS-denied Environments Most mobile mapping systems rely on GNSS as an absolute sensor to provide the link to a global reference system and compensate for the drift of the inertial sensors. However, in some environments, such as indoor areas, GNSS is unreliable or unavailable. This chapter briefly describes alternative sensing modalities and trajectory estimation concepts, which may replace or augment GNSS observations. Our key contributions in this context are:

1. The development of a sensor network, which can estimate the position of a person within an indoor environment based on (a) the network connectivity, (b) a human step detection algorithm using inertial sensors and (c) a floor plan of the environment. This information has been combined using a Particle Filter. The accuracy has been demonstrated to be in the order of a meter.

2. The development of an indoor localization system that uses estimates from a Chirp Spread Spectrum-based ranging system, a step detection procedure, and a floor plan.

3. The development of a foot-mounted sensor system that uses inertial sensors to update the pose estimation. The drift is compensated using zero-velocity and zero-angular rate updates and RFID and barometer readings. The system only uses low-cost sensors.

4. A procedure to use the laser scans from a mobile mapping system and city models to correct the trajectory of the mapping vehicle in an urban environment. Buildings were automatically detected from the scan data and matched to the information obtained from a city model database. This procedure can be used in cases where GNSS is unavailable or disturbed.

Chapter 4: High Precision Mobile Laser Scanning This chapter describes the development, calibration, and evaluation of mobile mapping systems, which use a high-grade IMU and a precise high-speed laser scanner to create dense and accurate point clouds from a moving platform. Our key contributions are:

1. A plane-based calibration environment and procedure to determine the transformation parameters between the laser scanner and the IMU with high accuracy.

2. An evaluation study on the accuracy of the resulting point clouds.

3. A study which evaluates the possibility of using the system to derive deformations of a road surface and to extract road-specific parameters.

Chapter 5: Mapping with UAVs When areas are not easily accessible by vehicles, UAVs can be used to map the environment. This chapter describes different systems and applications in the context of UAV based mapping. Our key contributions are:

1. The development of a sensor system that can calculate a UAV's pose accurately in real-time. This system allows a direct georeferencing of airborne images and can be used as an input to a structure-from-motion processing pipeline.

2. A method to integrate gyroscope data, fish-eye stereo camera images, and raw GNSS carrier phase observations to estimate the pose of a UAV.

3. A study on the usability of UAV image-based directly georeferenced point clouds for deformation analysis.

4. An investigation where UAV imagery and derived products have been used to characterize a solifluction lobe and its movement in an alpine glacier foreland.

5. A procedure to derive crop height data from UAV images. The procedures have been used in winter wheat breeding experiments to analyze the crop performance of different genotypes.

6. A study on the accuracy analysis of a UAV based laser scanning system.

Chapter 6: High-Throughput Phenotyping in Viticulture In viticulture, many monitoring actions, such as detecting diseases or counting berries to predict the yield, require manual work, take time, and are error-prone due to the subjectivity of the methods. This chapter describes a series of works that aim to automate parts of this process using an image-based mobile mapping system and the corresponding analysis pipelines.

1. The development of a senso system and a data processing pipeline to automatically create georeferenced overlapping images of the vine canopy.

The images are taken with a multicamera system mounted on a grapevine harvester while the vehicle drives through the vine rows.

2. A pipeline to count berries in the vine rows. The pipeline (a) creates 3D point clouds from the images, (b) segments berry points from the rest, (c) finds grape clusters and berries, and (d) counts berries and measures their diameter.

3. A method to automatically detect berries in single images using Convolutional Neural Networks.

4. A method to estimate the yield using multiple images from the sensor system and a study on its performance. The study uses data from 3 years, three varieties, and two different pruning systems.

Chapter 2

Inertial Navigation

The estimation of the trajectory of a moving platform is one of the crucial steps in mobile mapping. Since the goal of mobile mapping is usually a georeferenced map, the trajectory is needed with respect to a global coordinate system. Inertial sensors can be used to recursively determine the trajectory of a platform starting from a known initial pose without the need for any external reference information. This procedure is called *inertial navigation*, and it has been known for many decades. Because of the inherent drift of the inertial sensors and the necessary starting pose, inertial navigation usually integrates external corrective measurements such as GNSS or compass readings. This chapter briefly explains the sensors and algorithms behind inertial navigation. We also present sensor configurations, calibration procedures and algorithms, which we developed to minimize drift effects and systematic errors in trajectory estimation.

2.1 Coordinate Systems

In the context of inertial navigation are many coordinate systems involved. We, therefore, briefly define the different coordinate systems and the notation of kinematic quantities between the systems. Please note that we do not differentiate between coordinate frames and coordinate systems here and use both words equivalently.

Earth Centred Earth Fixed Global system attached to the Earth. The origin is in the mass centre of the Earth, the z-axis is parallel to the Earth's rotation axis, and the x-axis is going through the intersection of the Greenwich meridian (0° longitude) and the equatorial plane, the y-axis is completing a right-handed coordinate system. Coordinates in this system, as the position of a UAV, are usually written as $\mathbf{p}^e$.

Body Frame Local system attached to the moving platform. The origin is a point on the vehicle, e.g. the centre of mass, the x-axis is pointing forward, the z-axis is pointing down, and the y-axis is completing the right-handed system (pointing to the right). Please note that ground vehicles often have a different definition with z pointing up and y pointing to the left and that this is also often applied to UAVs. Coordinates in this system, as the position of a sensor on the platform, are usually written as $\mathbf{l}^b$.

Sensor Frame Local system attached to the sensor. Raw sensor readings are given in this system. Its definition strongly depends on the type of sensor. Coordinates in this system, as the position of an object detected by a scanner, are usually written as $\mathbf{x}^s$.

Navigation Frame Local topocentric system. The origin is the same as for the body frame, the x-axis is pointing towards North, the z-axis is pointing down (parallel to gravity), and the y-axis is completing the right-handed system, pointing East. This system is also called NED (North-East-Down). The rotation information about the UAV is usually given as a rotation $\mathbf{R}_b^n$ between the body frame and the navigation frame. If the UAV is levelled and the x-axis points north, the three rotation angles (roll, pitch, yaw) are (0,0,0). Please note that if the body frame is defined in a (Forward-Left-Up) mode, as it is usually for ground vehicles, the navigation frame is usually defined as (East-North-Up).

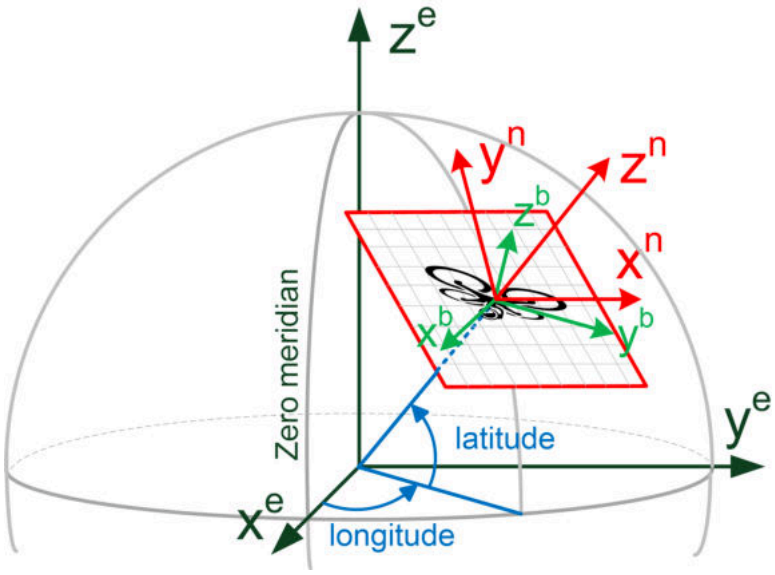

Figure 2.1: The connections between the global (e) coordinate system, the navigation (n) system and the platform (b) coordinate system.

Inertial Frame Global system attached to the universe. The origin and the z-axis are the same as for the ECEF-frame. The x and y-axis are tight to far-away celestial objects, considered fixed in the universe. The inertial frame is the reference for inertial sensors used for trajectory estimation. Coordinates in this frame are written as $\mathbf{x}^i$.

Notation To avoid ambiguities, kinematic quantities are accompanied by indices. Relative quantities, such as a velocity, are given as $\mathbf{v}_{ba}^c$, which means the "velocity of the system a relative to the system b, expressed in coordinates of the system c". A concrete example would be $\mathbf{v}_{eb}^n$, which is the velocity of the body system with respect to the Earth fixed system, expressed in the coordinates of the navigation frame. The rotation rate of the sensor with respect to the inertial frame, like a gyroscope measures it, would be $\boldsymbol{\omega}_{is}^s$ which is equal to the Earth rotation rate expressed in the sensor coordinate system $\boldsymbol{\omega}_{ie}^s$ if there is no additional rotation between the sensor and the Earth. A change of the resolving frame from system b to system c would be a transformation $\mathbf{T}_b^c$. An example is the rotation matrix $\mathbf{R}_b^n$ from the body frame to the navigation frame. Some indices are omitted if the context is evident or the reference system b and the resolving system c are the same.

2.2 Inertial Sensors

[**C13**] Schopp, P., **Klingbeil**, L., Peters, C., Buhmann, A., and Manoli, Y. (**2009**). Sensor fusion algorithm and calibration for a gyroscope-free IMU. *Procedia Chemistry*, 1(1):1323–1326

[**J21**] Schopp, P., **Klingbeil**, L., Peters, C., and Manoli, Y. (**2010**). Design, geometry evaluation, and calibration of a ggyroscope-free inertial measurement unit. *Sensors and Actuators A: Physical*, 162(2):379–387

[**J19**] Schopp, P., Graf, H., Maurer, M., Romanovas, M., **Klingbeil**, L., and Manoli, Y. (**2014**). Observing relative motion with three accelerometer triads. *IEEE Transactions on Instrumentation and Measurement*, 63(12):3137–3151

Inertial sensors build the core of most navigation systems because they provide information about the sensor's motion without the need for any external reference. Two types of sensors are considered inertial: accelerometers and gyroscopes (angular rate sensors). They measure the sensor's angular rates and non-gravitational accelerations with respect to the inertial frame. They are used to determine both translational and rotational components of the trajectory.

Accelerometers measure the specific force $\mathbf{f}_{is}^s$ acting on the sensor along its sensitive axis with respect to the inertial frame. The specific force is the non-gravitational force per unit mass, which is an acceleration. A three-axis ac-

celerometer free-falling from the sky would measure $0\,\mathrm{m\,s^{-2}}$ in any direction. An accelerometer, standing motionless on the ground, measures $9.81\,\mathrm{m\,s^{-2}}$ antiparallel to gravity, as this is the specific force of the ground acting on the sensor to prevent it from falling further down along the gravitational field of the Earth. The readings of a three-axis accelerometer can be used in two ways. In the case of a non-accelerating platform, it is possible to calculate two angles between the platform's z-axis and the gravity vector $\mathbf{g}_{grav}$ (rotations around the gravity vector are not observable). In the case of an accelerating platform, the gravitational and the translational acceleration components can be separated if the rotation of the platform is known, and the translational component can be integrated twice to derive the platform's position.

Gyroscopes or angular rate sensors measure the angular rate $\boldsymbol{\omega}_{is}^{s}$ of the sensor around its sensitive axis with respect to the inertial frame. The inertial frame is the coordinate system assumed to be fixed in the universe. As a consequence, a gyroscope lying motionless on the ground would still measure the Earth's rotation rate $\boldsymbol{\omega}_{ie}^{s}$. However, only high-grade gyroscopes are sensitive enough to measure the Earth's rotation. Starting from a known orientation and assuming that the gyroscope sensor coordinate frame is identical to the body frame, the three-axis angular rate sensor data can be integrated over time to derive the orientation R_b^n of the platform with respect to the navigation frame.

Inertial Measurement Units An Inertial Measurement Unit (IMU) is the combination of three accelerometers and three gyroscopes perpendicular aligned to cover all spatial axis. The readings from an IMU can be used to fully reconstruct the trajectory of a platform from a given starting position and orientation. This concept is called *strapdown integration* and is described below. Because the measurement errors add up during integration, the error of the resulting trajectory grows over time and needs to be corrected using sensor fusion methods.

Strapdown Integration Starpdown integration is the process of recursively calculating the a platforms position $\mathbf{p}_b^e$, velocity $\mathbf{v}_{eb}^n$, and orientation $\mathbf{C}_b^n$ based on a stream of inertial sensor data $\boldsymbol{\omega}_{ib}$ and $\mathbf{f}_{ib}$ and starting values $\mathbf{p}_0, \mathbf{v}_0, \mathbf{C}_0$:

$$[\mathbf{p}_b^e, \mathbf{v}_{nb}^e, \mathbf{C}_b^n]_k \;=\; f\left([\mathbf{p}_b^e, \mathbf{v}_{nb}^e, \mathbf{C}_b^n]_{k-1}, [\boldsymbol{\omega}_{ib}, \mathbf{f}_{ib}]_k\right). \tag{2.1}$$

One challenge in the method arises because inertial sensors measure with respect to the inertial system. At the same time, we are usually interested in positions and rotations with respect to the Earth system, which itself rotates with respect to the inertial system. Therefore, strapdown integration involves transformations

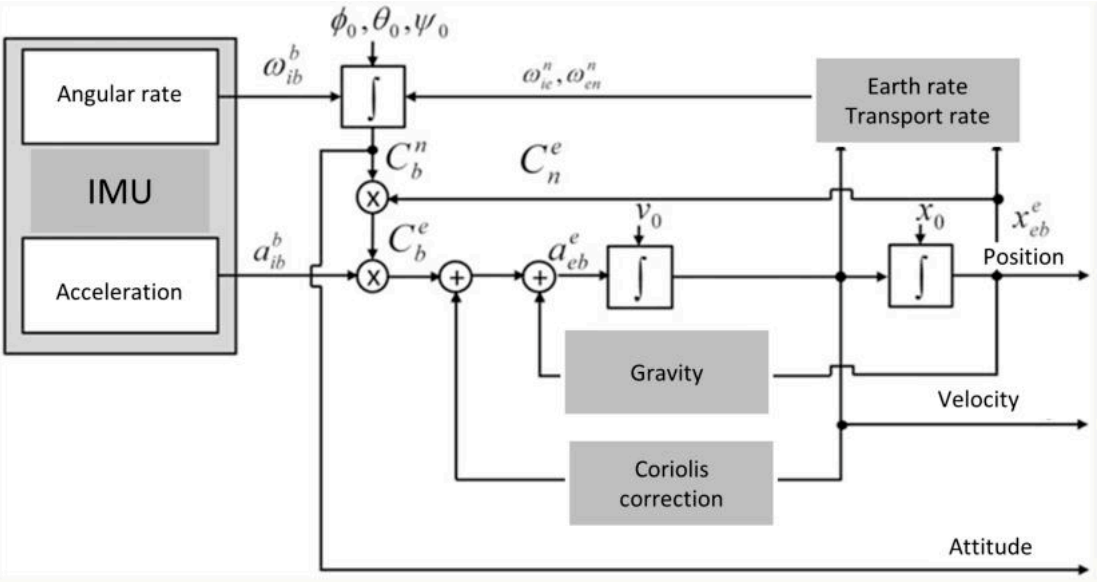

Figure 2.2: Schematic view of strapdown integration. Gyroscope and accelerometer outputs are integrated to update position, velocity and attitude.

between rotating reference frames and dealing with fictitious forces, such as Euler, Coriolis, and Centrifugal forces. Another complication is that accelerometers only measure non-gravitational accelerations, while gravitational forces also drive the velocity changes of an object and the resulting position changes. Therefore, a gravitation model and the object's orientation with respect to gravitation are needed.

Strapdown integration suffers from the accumulation of errors over time, resulting from the integration of noisy and biased inertial sensor readings. Additionally, the need for knowledge of the sensors orientation with respect to the gravity vector puts a special focus on the gyroscope sensor quality, as zero-rate offsets lead to a position error, which grows cubic with time.

Gyroscope-Free IMUs To address the drift problem, inherent to low-cost gyroscopes, we developed an IMU without a gyroscope ([C13], [J21], [J19]). These accelerometers are attached to distinct locations on the platform and build an accelerometer array. This concept is called *gyroscope-free IMU*. By knowing the relative position and orientation of the different accelerometers, the angular and translational acceleration and the angular velocity of the platform can be determined. The accuracy depends on the geometric configuration of the sensors. We describe algorithms to derive the motion from the sensor readings and present a method to calibrate the system by determining the relative positions and orientation of the sensors indirectly using a high precision 3D rotation table. We also used this table to evaluate the system performance.

2.3 Magnetometer

[J22] Wark, T., Corke, P., Sikka, P., **Klingbeil**, L., Ying, G., Crossman, C., Valencia, P., Swain, D., and Bishop-Hurley, G. (**2007**). Transforming agriculture through pervasive wireless sensor networks. *IEEE Pervasive Computing*, 6(2):50–57

[J18] **Klingbeil**, L., Eling, C., Zimmermann, F., and Kuhlmann, H. (**2014**a). Magnetic field sensor calibration for attitude determination. *Journal of Applied Geodesy*, 8(2):97–108

Another option to reduce drift effects in inertial navigation is the integration of magnetic field sensors. A three-axis magnetometer, measuring the vector $\mathbf{m}^s_{mag}$ of the Earth magnetic field $\mathbf{m}_{mag}$ in the local sensor frame, serves as a compass and provides information about the rotation of the platform around the gravity axis, which accelerometers cannot observe. This is why magnetometers are integrated into most inertial measurement units. A combination of gyroscope, accelerometer, and magnetometer theoretically allows deriving all three rotation angles between the body and navigation frames. However, the Earth's magnetic field in the close vicinity to vehicles is heavily disturbed by metallic components of the platform or superimposed by other mostly stronger field sources such as high currents driving the engines, in the case of UAVs. Therefore, the usage of magnetic field sensors has to be considered carefully, as they may cause more problems than they solve.

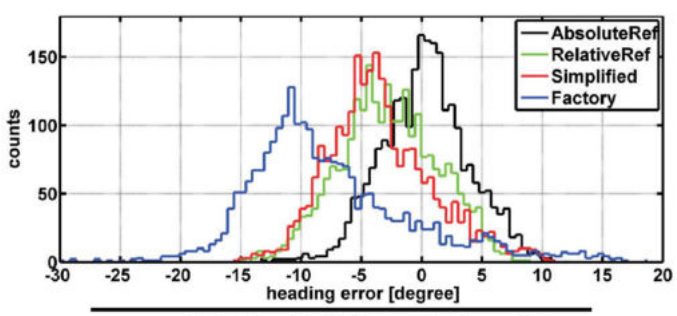

	Abs.Ref	Rel.Ref	Simpl.	Factory
mean	0.0517	-2.9476	-3.6522	-7.7819
std	3.6227	4.0932	4.3959	6.9666

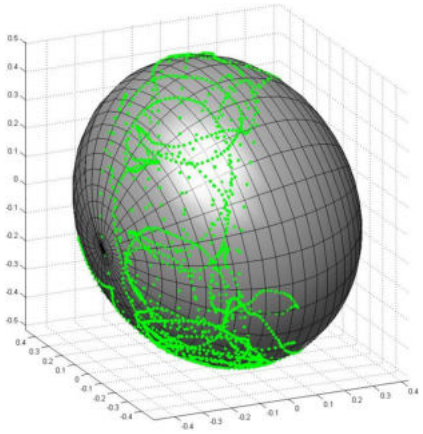

Figure 2.3: Magnetometer calibration. The left side shows the orientation error distribution after different calibration versions. The right side shows the magnetometer vector readings during the calibration procedure [J18].

Magnetometer Calibration As mentioned above, magnetic field sensors are susceptible to local disturbances of the Earth's magnetic field, which may be induced by ferromagnetic material in the vicinity of the sensor. In [J22] and [J18], we developed a method to calibrate magnetic disturbances, which are caused by metallic or magnetic objects on the platform. The procedure also compensates

constant internal sensor errors, such as scale factors, biases, and axis misalignment. No particular measurement setup is needed. The only necessary assumption is a temporally and spatially constant Earth magnetic field vector in the calibration environment. In this case, the disturbances and calibration errors force the sensor readings to lie on an ellipsoid, and the calibration parameters can derived from the ellipsoid parameters. In [J18], we also evaluated the quality of the calibration result. We showed that some simplifications, which make the calibration procedure easier to use, have no significant impact on the results.

2.4 Global Navigation Satellite Systems

[C6] Zimmermann, F., Eling, C., **Klingbeil**, L., and Kuhlmann, H. (**2017**). Precise positioning of UAVs - dealing with challenging RTK-GPS measurement conditions during automated UAV flights. *ISPRS Annals of the Photogrammetry, Remote Sensing and Spatial Information Sciences*, 4:95–102

[J11] Zimmermann, F., Holst, C., **Klingbeil**, L., and Kuhlmann, H. (**2018**). Accurate georeferencing of TLS point clouds with short GNSS observation durations even under challenging measurement conditions. *Journal of Applied Geodesy*, 12(4):289–301

[J8] Zimmermann, F., Schmitz, B., **Klingbeil**, L., and Kuhlmann, H. (**2019**). GPS multipath analysis using fresnel zones. *Sensors*, 19(1):25

Inertial sensor and strapdown integration need an initial pose in a global coordinate system to provide a suitable trajectory for georeferencing. They also suffer from drift effects. Inertial navigation systems and algorithms usually integrate Global Navigation Satellite System (GNSS) observations to address both problems. With a GNSS, it is possible to determine the position $\mathbf{x}_s^e$ of a GNSS antenna with respect to a global coordinate system by measuring the time of flight of the signals between satellites at known positions and the antenna. Additionally, the receivers can measure Doppler shifts of the signals and the velocity $\mathbf{v}_{es}^e$ of the antenna. The whole concept comes with many errors and uncertainties, such as satellite position and clock errors, receiver clock errors, signal refraction in the atmosphere and signal disturbances in the receiver environment. Several possible GNSS processing options differ mainly in the used observations and the methods to reduce or eliminate the abovementioned errors. The most commonly used processing mode, especially in mobile mapping applications, is the Real-Time Kinematic (RTK) mode. RTK uses the phase shift of the carrier waves of the GNSS signal between the transmitter and the receiver as observations. Due to the periodic nature of the electromagnetic wave, this observation comes with ambiguities, which need to be solved during the position estimation process. It also uses differential measurements, which means that the used observations are differences between the carrier phase observations at two receivers, one placed at a known position (master) and one at the vehicle (rover). Building differences

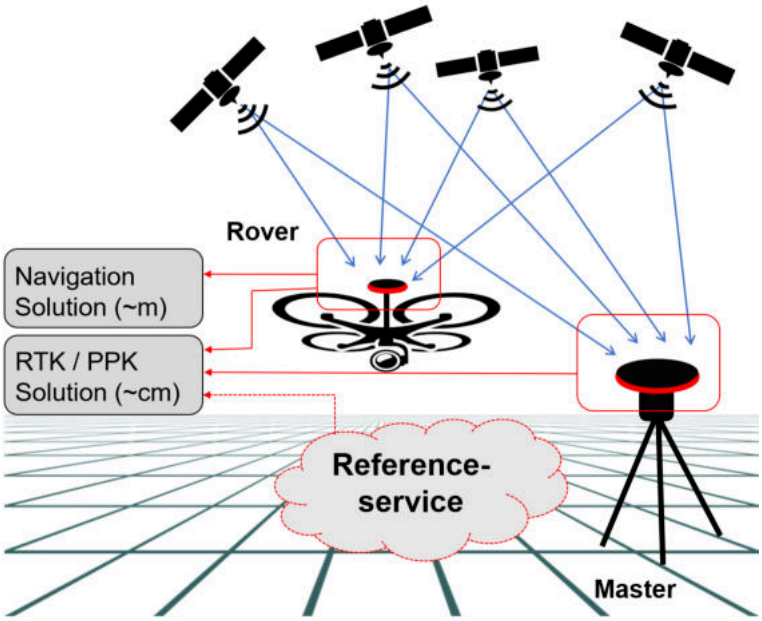

Figure 2.4: Commonly used GNSS processing options. The data from a master station or a reference service are used to correct the rover observations, either online or offline after the measurements have been obtained.

reduces or eliminates most of the errors mentioned above and enables a position accuracy of the rover relative to the master in the order of centimetres, given that the ambiguities have been successfully solved. A drawback of RTK GNSS is that the observations of the master need to be available at rover, which usually involves an internet connection or radio link if the position is needed in real-time.

Satellite Selection Strategies One of the largest sources of systematic errors in GNSS is the geometric structure of the antenna environment (Fig. 2.5 (left)). Apart from the direct observation of signals coming from the satellite and a total blocking of signals by buildings, also mixed effects can appear, such as overlapping of direct and reflected signals (*multipath effects*) and the sole reception of reflected or diffracted signals (*none-line-of-sight effects*). Both types of effects can lead to errors of several meters and can not be reduced by differential processing modes, such as RTK. They are very prominent in urban areas, where reliable position information is often required. In [C6], [J11], and [J8], we developed procedures to investigate the influence of multipath and non-line-of-sight effects on the position estimate using the knowledge about the environment, the own position, and the position of the satellites. By doing so, we can better plan the trajectory or select unaffected satellites. Both significantly improve the quality of the localization results.

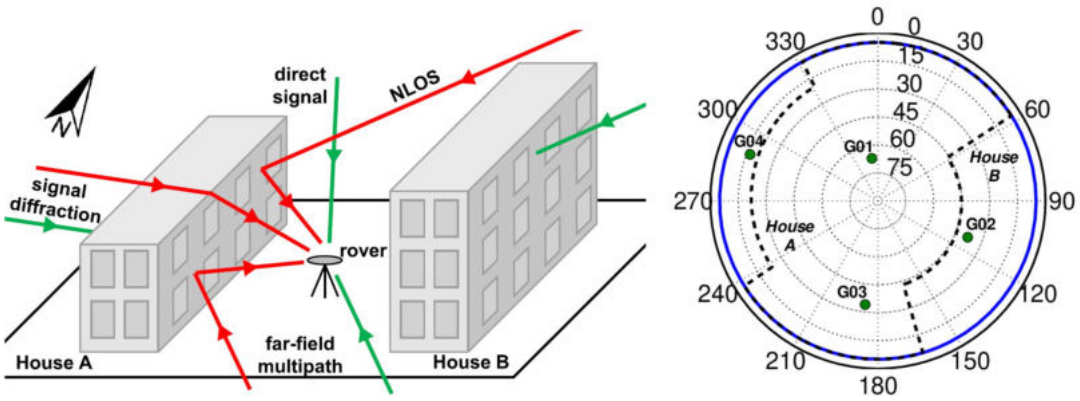

Figure 2.5: Left: Multipath and non line of sight effects in urban environments. Right: Unaffected satellites can be selected to improve the results.

2.5 State Estimation Algorithms

[C14] Romanovas, M., **Klingbeil**, L., Trächtler, M., and Manoli, Y. (**2009**). Efficient orientation estimation algorithm for low cost inertial and magnetic sensor systems. In *2009 IEEE/SP 15th Workshop on Statistical Signal Processing*. IEEE

[J17] Eling, C., **Klingbeil**, L., and Kuhlmann, H. (**2015**a). Real-time single-frequency GPS / MEMS - IMU attitude determination of lightweight UAVs. *Sensors*, 15(10):26212–26235

So far, we showed that the observations from the inertial sensors can be used to calculate the trajectory and that their relative nature leads to a growing drift over time. We also explained, that GNSS receivers or magnetometers can provide absolute position or orientation observations, which, however, may contain stochastic or systematic errors. It is important to combine all the different sensors in the best possible way, leveraging the specific advantages of the different sensors to minimize the overall estimation error. This procedure can be formalized as a state estimation problem, where the state at each time step consists of the position and orientation of the vehicle and potentially other parameters, which may be necessary to model the behaviour of the state over time. One option to solve the state estimation problem is to use Recursive Bayesian Estimation (RBE).

Recursive Bayesian Estimation A Recursive Bayesian Estimation (RBE) algorithm is used to estimate the state $\mathbf{x}_k$ of a system at the time t_k based on all measurements $Z_k = \{\mathbf{z}_0, \ldots, \mathbf{z}_k\}$ up to that time. The state estimation is represented as a probability density function $p(\mathbf{x}_k \mid \mathbf{z_0}, \ldots, \mathbf{z_k})$, which can be calculated using Bayes' Rule:

$$p(\mathbf{x}_k \mid Z_k) = \frac{p(Z_k \mid \mathbf{x}_k) p(\mathbf{x}_k)}{p(Z_k)}, \tag{2.2}$$

which can be transformed into a recursive equation:

$$p(\mathbf{x}_k \mid Z_k) = \frac{p(\mathbf{z}_k \mid \mathbf{x}_k)p(\mathbf{x}_k \mid Z_{k-1})}{p(\mathbf{z}_k \mid Z_{k-1})} = \eta \cdot p(\mathbf{z}_k \mid \mathbf{x}_k)p(\tilde{\mathbf{x}}_k).$$

The term $\eta = p(\mathbf{z}_k \mid Z_{k-1})$ is a normalization factor. The term $p(\mathbf{x}_k \mid Z_k)$ is called the *a posteriori* probability and describes the current state estimate using all measurements up to now. The term

$$p(\tilde{\mathbf{x}}_k) = p(\mathbf{x}_k \mid Z_{k-1}) = \int p(\mathbf{x}_k \mid \mathbf{x}_{k-1})p(\mathbf{x}_{k-1} \mid Z_{k-1})dx_{k-1}$$

is called *a priori* probability and describes the current estimate using all but the current measurement. It contains the a posteriori estimation $p(\mathbf{x}_{k-1} \mid Z_{k-1})$ of the last time step and the term $p(\mathbf{x}_k \mid \mathbf{x}_{k-1})$, which represents the *process model* describing the knowledge about the dynamics of the system and the corresponding uncertainties. The term $p(\mathbf{z}_k \mid \mathbf{x}_k)$ represents the *measurement model* and relates the measurements to the state, considering also the sensor uncertainties. Having all these terms in mind, any recursive Bayesian estimation cycle is performed in two steps. In the *prediction step* the a priori probability is calculated from the last a posteriori probability using the process model (Eq. 2.3). In the *correction step* the a posteriori probability is calculated from the a priori probability using the measurement model (Eq. 2.3) and the current observation.

Kalman Filters When using a *Kalman Filter*, it is assumed, that the probability distribution $p(\mathbf{x}_k)$ of the state vector at a time t_k is Gaussian and can be represented by the mean $\mathbf{x}_k$ and the covariance $\mathbf{P}_k$. It is also assumed, that the temporal evolution of the state can be modelled as

$$\mathbf{x}_k = f_k(\mathbf{x}_{k-1}, \mathbf{u}_k, \mathbf{w}_k), \qquad \mathbf{w}_k \sim \mathcal{N}(\mathbf{0}, \mathbf{Q}_k), \tag{2.3}$$

with $\mathbf{u}_k$ being a deterministic control input to the system and $\mathbf{w}_k$ being normally distributed noise, representing the uncertainty of the model. An observation $\mathbf{z}_k$ of the state can be described by

$$\mathbf{z}_k = h_k(\mathbf{x}_k, \mathbf{v}_k), \qquad \mathbf{v}_k \sim \mathcal{N}(\mathbf{0}, \mathbf{R}_k), \tag{2.4}$$

with $\mathbf{v}_k$ being normally distributed measurement noise.

Using the Jacobi matrices

$$\mathbf{\Phi}_k = \frac{\partial f_k(\mathbf{x}, \mathbf{u}, \mathbf{w})}{\partial \mathbf{x}} \qquad \mathbf{B}_k = \frac{\partial f_k(\mathbf{x}, \mathbf{u}, \mathbf{w})}{\partial \mathbf{u}} \qquad \mathbf{H}_k = \frac{\partial h_k(\mathbf{x})}{\partial \mathbf{x}} \tag{2.5}$$

the Kalman Filter equations can be derived from the RBE equations as follows.

$$\begin{aligned}
\mathbf{x}_k^- &= f_k(\mathbf{x}_{k-1}, \mathbf{u}_k) \\
\mathbf{P}_k^- &= \mathbf{\Phi}_k \mathbf{P}_{k-1} \mathbf{\Phi}^T + \mathbf{Q}_k \\
\mathbf{K}_k &= \mathbf{P}_k^- \mathbf{H}_k^T (\mathbf{H}_k \mathbf{P}_k^- \mathbf{H}_k^T + \mathbf{R}_k)^{-1} \\
\mathbf{x}_k &= \mathbf{x}_k^- + \mathbf{K}_k (\mathbf{z}_k - h_k(\mathbf{x}_k^-)) \\
\mathbf{P}_k &= (\mathbf{I} - \mathbf{K}_k \mathbf{H}_k) \mathbf{P}_k^-
\end{aligned}$$

This is possible because Gaussian distributions stay Gaussian after linear transformations. In cases where the models h_k and f_k are linear with respect to the state vector and the control inputs, the derivation of the matrices $\mathbf{\Phi}_k, \mathbf{B}_k$ and $\mathbf{H}_k$ is exact and not an approximation at a particular linearization point. Then the Kalman Filter is an optimal solution, minimizing the estimation error in the least square sense. If the models are non-linear and need to be linearized, as shown above, the algorithm is called *Extended Kalman Filter* (EKF). The estimate, in this case, is an approximative solution. An alternative approach to deal with non-linear models is to represent the mean and the covariance by some deterministically chosen points, transform them using the non-linear functions f_k and h_k and recover the mean and covariance back from the transformed points. This approach is used in the *Unscented Kalman Filter* (UKF), with very similar equations to the ones shown above.

Particle Filters A Particle Filter (PF) is an alternative approach to deal with the heavy integrals of the RBE equations. It is a Monte Carlo Simulation-based approach, where many random sample points represent the probability distribution. All transformations of the probabilities are then calculated using those samples. In this case, no assumption about the nature of the distribution and no linearization of the models is necessary. Particle Filters have the advantage that non-linear processes and observation models can be implemented without linearization. Also, arbitrary non-Gaussian and multi-modal distributions can describe the uncertainties. A disadvantage of the PF is that for higher dimensional state spaces, as the full 6D pose of an object, the number of needed particles is very high, leading to a high computational burden. However, in lower-dimensional cases, as shown in Ch. 3, it is often applied.

Efficient Kalman Filtering For Orientation Estimation Using a 3-axis gyroscope, it is possible to derive the 3D orientation of a platform by integrating the angular rates from known start values. Especially for low-cost devices, sensor errors accumulate very fast over time. An accelerometer can compensate for roll and pitch drifts by observing the Earth's gravitational field, but this is only

possible in stationary phases. The yaw drift can be compensated by using a magnetometer. In [C14] we developed a Kalman filter, which is capable of estimating the orientation of an object even for high dynamic movements.

The state vector $\mathbf{x}_k$ consists of the orientation of the object, represented by a quaternion $\mathbf{q}$, the gyroscope bias $\mathbf{b}$ and the translational acceleration $\mathbf{a}$. We treat the angular rate $\boldsymbol{\omega}$ a control input $\mathbf{u}$ and write the process model as

$$\mathbf{x}_k = \begin{bmatrix} \mathbf{q}_k \\ \mathbf{b}_k \\ \mathbf{a}_k \end{bmatrix} = f\left(\mathbf{x}_{k-1}, \mathbf{u}_k\right) = \begin{bmatrix} \mathbf{q}_{k-1}\mathbf{q}_\Delta(\boldsymbol{\omega}_k) \\ \mathbf{b}_{k-1} \\ \gamma\mathbf{a}_{k-1} \end{bmatrix}, \tag{2.6}$$

where $\mathbf{q}_\Delta$ corresponds to the differential rotation calculated from the angular rate. The parameter $\gamma \leq 1$ parameterize the acceleration dynamics, assuming that it converges to zero on the long run.

We include the specific force $\mathbf{f}$ measured by the accelerometer and the magnetic field measurement $\mathbf{m}$ via the measurement model.

$$\mathbf{z}_k^f = \mathbf{q}_k \left(\mathbf{G}^e - \mathbf{a}_k\right) \mathbf{q}_k^{-1}, \tag{2.7}$$

$$\mathbf{z}_k^m = \mathbf{q}_k \mathbf{M}^e \mathbf{q}_k^{-1}. \tag{2.8}$$

Here, $\mathbf{G}^e$ and $\mathbf{M}^e$ are the Earth's gravitational acceleration vector and the Earth's magnetic field vector in the target coordinate system. We realized the filter in the form of an Unscented Kalman Filter.

Kalman Filter for Full Pose Estimation For full pose estimation, additional measurements, such as GNSS, are necessary to compensate for the velocity and position drift. In [J17] we developed algorithms for full pose estimation of a UAV. We use a classical inertial navigation approach as a basis for the estimation. The state vector contains the position $\mathbf{p}$, the orientation $\mathbf{C}$ and the velocity $\mathbf{v}$. Because the biases $\mathbf{b}_\omega$ and $\mathbf{b}_f$ of the gyroscopes and the accelerometers usually change slowly and non-deterministically, we estimated them as part of the state vector:

$$\mathbf{x} = \left[\mathbf{p}, \mathbf{v}, \mathbf{C}, \mathbf{b}_\omega, \mathbf{b}_f\right]. \tag{2.9}$$

We implement the process model by applying the strapdown integration algorithm as described above using inertial sensor readings $\boldsymbol{\omega}$ and $\mathbf{f}$, which have been corrected using the current estimates of the inertial sensor biases.

To reduce inertial sensor drift, we realized a short GNSS baseline on the UAV by mounting two antennas at a distance of about 1 m. In the observation model, we create the observation $\mathbf{z}^\mathbf{B}$ of the GNSS baseline vector $\mathbf{B}^n$ in the navigation frame by transforming the known vector $\mathbf{B}^b$ in the body frame using the current estimate of the orientation $\mathbf{C}_b^n$:

$$\mathbf{z}^\mathbf{B} = \mathbf{C}_b^n \mathbf{B}^b.$$

We implemented our own baseline processing algorithm, which was optimized for the particular sensor setup measurement conditions and also included the ambiguity resolution. By this, we were able to increase the success rate and the time to fix the ambiguities significantly and avoided the need for magnetometer observations to stabilize the heading angle. Magnetometer measurements are heavily disturbed on UAVs due to the magnetic fields induced by the strong currents driving the engines. Fig. 2.6 shows the estimation improvement when the rotational drift is compensated using the second GNSS antenna. The setup on the left of the figure was used to investigate the estimation accuracy.

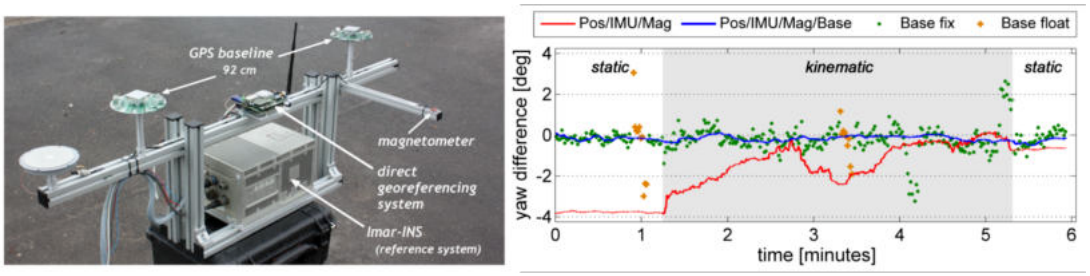

Figure 2.6: Left: Evaluation of an attitude estimation method using a short single-frequency GPS baseline. Right: Yaw measurements from a short GPS baseline and their benefit in attitude estimation [J17].

Chapter 3

Localization in GNSS-Denied Environments

[C16] **Klingbeil**, L., Wark, T., and Bidargaddi, N. (**2007**). Efficient transfer of human motion data over a wireless delay tolerant network. In *2007 3rd International Conference on Intelligent Sensors, Sensor Networks and Information (ISSNIP)*. IEEE

[C15] **Klingbeil**, L. and Wark, T. (**2008**). A wireless sensor network for real-time indoor localisation and motion monitoring. In *2008 International Conference on Information Processing in Sensor Networks (IPSN)*. IEEE

[C12] **Klingbeil**, L., Romanovas, M., Schneider, P., Traechtler, M., and Manoli, Y. (**2010**). A modular and mobile system for indoor localization. In *2010 International Conference on Indoor Positioning and Indoor Navigation (IPIN)*. IEEE

[C11] Romanovas, M., Goridko, V., **Klingbeil**, L., Bourouah, M., Al-Jawad, A., Traechtler, M., and Manoli, Y. (**2013**). Pedestrian indoor localization using foot mounted inertial sensors in combination with a magnetometer, a barometer and RFID. In *Lecture Notes in Geoinformation and Cartography*, pages 151–172. Springer Berlin Heidelberg

[C7] Schneider, J., Eling, C., **Klingbeil**, L., Kuhlmann, H., Förstner, W., and Stachniss, C. (**2016**). Fast and effective online pose estimation and mapping for UAVs. In *2016 IEEE International Conference on Robotics and Automation (ICRA)*. IEEE

[J3] Lucks, L., **Klingbeil**, L., Plümer, L., and Dehbi, Y. (**2021**). Improving trajectory estimation using 3D city models and kinematic point clouds. *Transactions in GIS*, 25(1):238–260

In Ch. 2 we presented the more classical approach of fusing inertial sensor data with GNSS observations to derive the platform trajectory. GNSS integration limits the drift of the IMU, and a position accuracy in the order of centimetres can be achieved, depending on the GNSS processing mode and measurement conditions. A challenge remains in areas where GNSS is strongly disturbed or unavailable, such as indoor environments. There are several possible options to deal with the lack of reliable GNSS measurements:

1. Use other less-drifting methods of motion prediction than strapdown integration.

2. Use other sensor modalities to derive position or distance information.

3. Use additional information about the environment or the motion to constrain possible trajectories and limit drift.

4. Use the sensors observing the environment, such as camera or laser scanners, as additional sensors for trajectory estimation.

This chapter presents some concepts and examples of these options to enable localization in indoor or outdoor environments where GNSS was not or barely available.

3.1 Dead-Reckoning

The strapdown approach to predict the trajectory using inertial sensors shows drift effects, especially for lower quality sensors. Depending on the type of the platform and the available sensors, an alternative method would be the dead reckoning approach, especially if only the 2D position is needed. Here, the 2D position $\mathbf{p}_k$ of an object at a time t_k can be calculated from the previous position $\mathbf{p}_{k-1}$, a travelled distance s_k since the last time step and a moving direction ϕ_k:

$$\mathbf{p}_k = \mathbf{p}_{k-1} s_k \begin{pmatrix} \cos\phi_k \\ \sin\phi_k \end{pmatrix}. \tag{3.1}$$

Depending on the available sensor, the traveled distance can also be calculated from a speed measurement and the time difference:

$$s_k = v_k \Delta t. \tag{3.2}$$

Similarly, the moving direction can be calculated by updating an initial direction ϕ_0 with measurements ω of angular rates:

$$\phi_k = \phi_{k-1} + \omega_k \Delta t. \tag{3.3}$$

As for strapdown integration, the problem with dead reckoning is that measurement errors of the relative sensor observations add up, and the uncertainty of the position estimate becomes more significant over time. Nevertheless, dead reckoning is often used as part of the position estimation procedure for robotic vehicles and pedestrians.

Pedestrian Step Detection In [C15] and [C16] we developed a pedestrian dead reckoning system. We used a sensor unit containing an IMU and a magnetometer which a person is carrying on their waist (Fig. 3.1 left). The step detector

used the readings of the three-axis accelerometer as an input to a threshold-based detection algorithm (Fig. 3.1 right). We then assumed the person to have a certain step length, which allows the calculation of the travelled distance. Together with a direction measurement coming from the gyroscopes and the magnetometer, the trajectory of a walking person can be calculated. Due to wrong detected

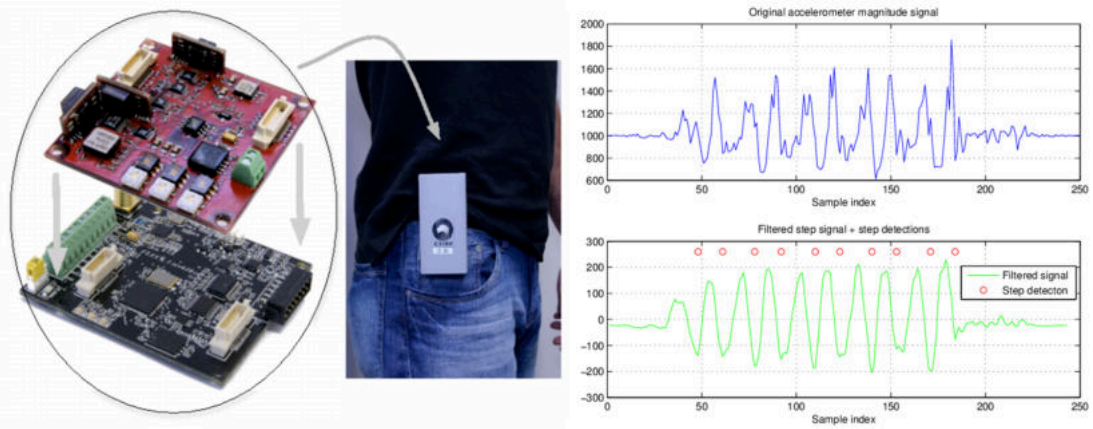

Figure 3.1: Waist worn sensor system (left), which is used to detect steps of person. Accelerometer values are fed to a threshold based detection algorithm (right).

steps, the constant step length assumption, and magnetic field disturbances, the resulting trajectory will still show drift effects. Other sensor modalities may help to correct those in GNSS-denied environments.

3.2 Radio Ranging and Proximity Sensing

GNSS provide a valuable option to derive the platform position in a global coordinate system using radio-based ranging to known satellite positions in outdoor environments. Other radio-based methods aim for similar functionality in areas where GNSS is unavailable, such as indoor areas. *Pseudolites* are similar to GNSS satellites, following the same measurement concept using ground-based transmitters. *Ultra-wideband systems* are deployed in indoor environments, such as industrial facilities, and they also use signal transmission times to estimate the distance between transmitters and receivers. While the latter methods need a dedicated installation for the localization purpose, other methods exploit existing WiFi infrastructure. Some estimate the distance to access points using the received signal strength, or they learn signal strength patterns in the environment and deduce the most probable location using machine learning methods. Another method to generate an absolute position measurement is to detect the proximity to a Bluetooth or RFID tag, which is placed at a known location.

Network Transmission Rate as Distance Sensors In [C15] and [C16], we used the packet transmission rate with two sensor nodes in a sensor network as an indicator for the maximum distance between the nodes. As shown on the left side

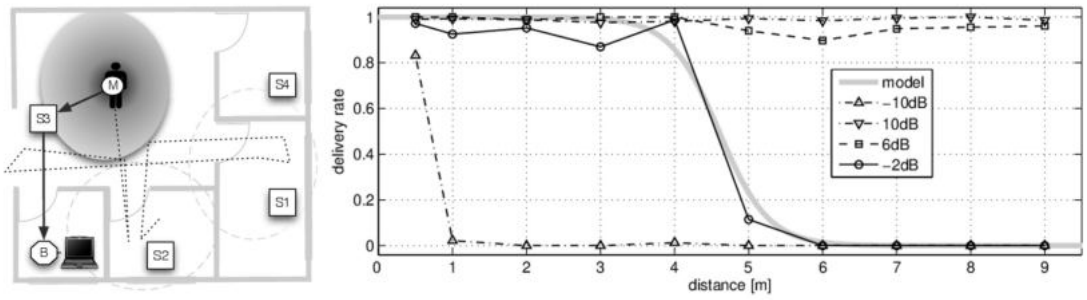

Figure 3.2: Distance measurement using network transmission rate [C15][C16]. Room setup with several access points (left). Network delivery rate for different distances and gain settings (right).

in Fig. 3.2, a node attached to a person moving through an indoor environment constantly exchanges data packets with static nodes via a radio channel. Based on the percentage of successfully transmitted packages, we derive an estimate of the proximity between the nodes (Fig. 3.2 right). Although the information is not very accurate and has systemtic errors due to the radio propagation properties in indoor spaces, it can still be used to improve the localization quality. This is shown later.

Radio Ranging in Indoor Environments In [C12], we used a radio-based ranging concept to locate a person in an indoor environment. Similar to the example above, a mobile sensor network node is communicating with static nodes in an indoor environment (Fig. 3.3 left). In this example, the radio channel uses

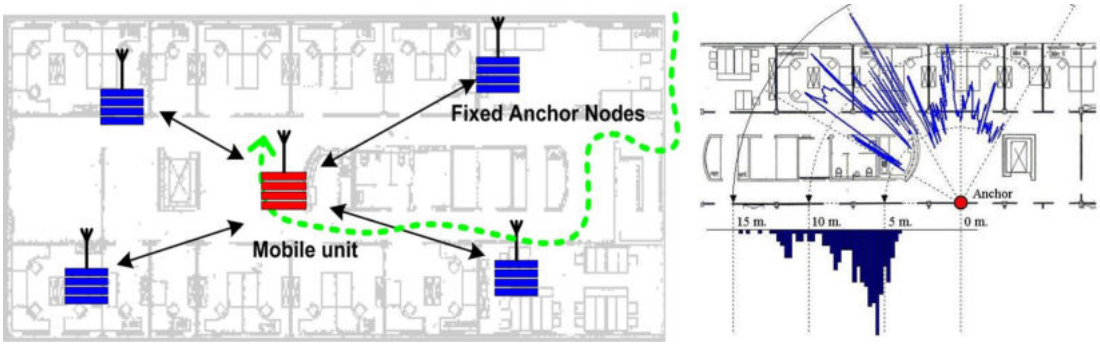

Figure 3.3: Indoor environment with multiple anchor nodes (left). Distribution of range measurements for 5 m distance [C12].

a chirp spread spectrum technology for communication, which also allows to measure the signal flight time and, therefore, the distance between the nodes.

According to the manufacturer, the distance accuracy is several centimetres. It can be seen that the measurement usually overestimates the actual distance due to signal reflections on the walls. The error distribution has a tail towards higher distances. However, as shown in the paper, this distribution can be considered in the position estimation algorithm.

3.3 Integration of Constraints

Another option to reduce drift from dead reckoning or strapdown integration is leveraging knowledge about the environment into the estimation process. One example is the usage of maps to limit the possible motion of the object and therefore create boundaries for the estimation. Another option is to integrate knowledge about the motion itself. If the object is detected to be static by some detection algorithm, the velocity is known to be zero in this situation. This knowledge can constrain the motion model in the estimation process using a so-called *zero-velocity update*.

Map Constraints In [C12] and [C15], we implemented Particle Filters to estimate the 2D position of a person in an indoor environment. We combined a step detector as described above with radio ranging and proximity sensing and a map of the environment. The map is utilized to limit the drift of the motion estimate. The state vector consists of the 2D position of the person in a topocentric coordinate system. The process model is realized as a dead-reckoning approach. Each step, which is detected by a waist-worn sensor unit, triggers a particle's motion in the direction of a corresponding magnetometer based heading measurement. This motion is applied to all particles, each with slightly different values for the step length and the heading direction. This distribution represents the uncertainty of the model. At this point, we also integrated the map of the environment, which

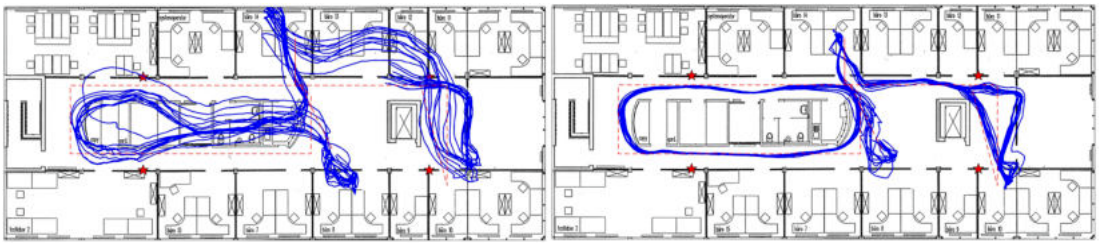

Figure 3.4: Indoor trajectory without (left) and with (right) integration of map information[C12].

we represented as an occupancy grid. We checked if a particle moves through a walkable area for each detected step. If not, we set the weight of this particular particle to zero, representing a lower probability of people walking through walls.

Additionally, we updated the probability of each particle according to the range observations and their uncertainty in the correction step. Fig. 3.4 illustrates, how the map limits the drift of the trajectory within an office environment. Here, the trajectory has been recovered from the particle distribution by building the mean for each time step.

In [C12], we used the transmission rate from the sensor unit to a fixed anchor node to update the probabilities. In [C15], we used a radio-based distance measurement. The above examples describe situations where a PF is a good choice of estimation algorithm because of the low dimensionality of the state space, the non-linearity of the process model, the non-Gaussian observation models and the simple possibility of integrating the map of the environment.

Zero-Velocity Updates In [C11] we present a pedestrian indoor localization system, which is based on a foot mounted-sensor, containing a low-cost IMU, a magnetometer and an RFID reader. The position and orientation of the foot are calculated using a classical strapdown integration approach, as presented in Sec. 2.2. Whenever we detect the no-motion stance phase of the foot on the ground, we create pseudo-observation for the angular rates $\mathbf{z}^{\omega}$ and the velocities $\mathbf{z}^{\mathbf{v}}$:

$$\mathbf{z}^{\omega} = [0,0,0]^T, \tag{3.4}$$

$$\mathbf{z}^{\mathbf{v}} = [0,0,0]^T. \tag{3.5}$$

These observations enable direct observation of the gyroscope bias and set a potential velocity drift to zero. We also integrated acceleration measurements as in Eq. 2.7, knowing that the translational acceleration is zero during that time. Additionally, we integrated several RFID tags, which we deployed at known positions $\mathbf{p}^i_{RFID}$ into the localization process by triggering and observation of the corresponding position whenever the tag reader detected the tag i:

$$\mathbf{z}^{\mathbf{p}} = \mathbf{p}^i_{RFID}. \tag{3.6}$$

Fig. 3.5 (left) shows, how different pseudo observations, resulting from the stance phase detection reduce the drift of the trajectory estimation. The right part of the figure shows the estimation result in an indoor environment. Note, that in all graphs only inertial sensors are used.

3.4 Use of Mapping Sensors for Navigation

Most sensors explained above are navigation sensors, meaning that their actual purpose is to measure information about the motion state of the platform in

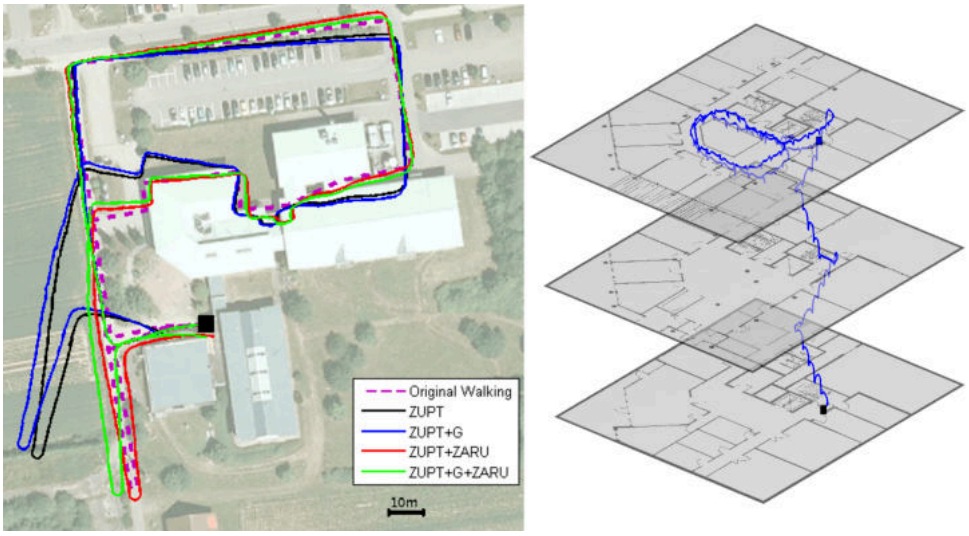

Figure 3.5: Effect of different pseudo-observations on the estimated trajectory (left). Multi-storey indoor trajectory estimation (right). [C11].

order to derive the needed trajectory parameters, such as position and orientation with respect to the target coordinate frame. However, it is also possible to use the mapping sensors to derive information about the platform trajectory. Some of these methods are described in the following, focusing on cameras and laser scanners as mapping sensors.

Cameras When a sufficient number of features is visible in two images, the relative transformation between the two camera poses can be calculated. When a camera is attached to a platform, these transformations, calculated for consecutive images, can be considered measurements of the relative motion of the vehicle. Using these measurements to recursively update the vehicle's pose from a known starting position is called *visual odometry*. The quality of the results depends on the type of motion, the camera's viewing direction, and the visual appearance of the environment. Visual odometry suffers from drift similar to dead reckoning and inertial integration. In [C7] we presented a procedure where two stereo fisheye camera pairs were used to calculate the trajectory of a UAV using an incremental bundle adjustment approach. Although our main contribution to this work was integrating GNSS carrier phase observation into the procedure, the paper may still serve as an example of using cameras for trajectory estimation.

Laser Scans A very similar measurement can be generated by observing consecutive laser scans when the scanner is attached to a vehicle that moves through an otherwise static environment. The relative transformation can be estimated if two scans have sufficient spatial overlap. This procedure is often called *scan matching* and is mainly realized using an iterative closing points (ICP) algorithm.

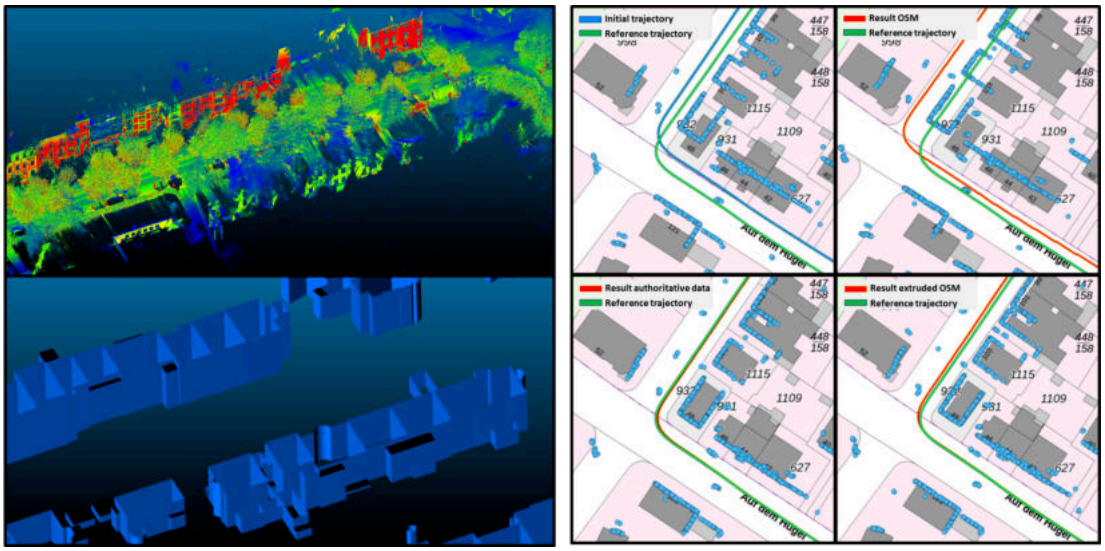

Figure 3.6: Using City Models to improve accuracy. The left side shows the recorded point cloud of a city street and the corresponding city model. The right side shows, how the city models from different sources can improve the result. See [J3] for more details.

The resulting information can be used in the same way as in the case of visual odometry.

Another option to use the laser scans to derive information about the trajectory is to match the sensor readings with some previously known or simultaneously estimated environment map. The paper [J3] shows how we used the result of a kinematic laser scanning process to improve the underlying trajectory. We created an initial point cloud using an approximate solution of the trajectory. Within this point cloud, we automatically detect planes of building facades and match them to the polygons of an existing LOD2 city model. We used the matching transformations as constraints or additional measurements to a new iteration of the trajectory estimation process. This improves the results, assuming that the city model has better accuracy than the initial approximate solution. Especially in regions with significant systematic errors, as they can quickly occur in urban environments due to GNSS multipath and non-line-of-sight effects.

Chapter 4

High Precision Mobile Laser Scanning

[**J16**] Heinz, E., Eling, C., Wieland, M., **Klingbeil**, L., and Kuhlmann, H. (**2015**). Development, calibration and evaluation of a portable and direct georeferenced laser scanning system for kinematic 3D mapping. *Journal of Applied Geodesy*, 9(4):227–243

[**C4**] Heinz, E., Eling, C., Wieland, M., **Klingbeil**, L., and Kuhlmann, H. (**2017**). Analysis of different reference plane setups for the calibration of a mobile laser scanning system. In Lienhart, W., editor, *Ingenieurvermessung 17, Beiträge zum 18. Internationalen Ingenieurvermessungskurs, Graz, Austria*, pages 1–14. Wichmann Verlag

[**J10**] Heinz, E., Eling, C., **Klingbeil**, L., and Kuhlmann, H. (**2019**). On the applicability of a scan-based mobile mapping system for monitoring the planarity and subsidence of road surfaces - pilot study on the A44n motorway in germany. *Journal of Applied Geodesy*, 14(1):39–54

[**J7**] Heinz, E., Holst, C., Kuhlmann, H., and **Klingbeil**, L. (**2020**). Design and evaluation of a permanently installed plane-based calibration field for mobile laser scanning systems. *Remote Sensing*, 12(3):555

In the previous chapters, we presented some general concepts of trajectory estimation and our contributions within this context. This chapter presents the development of a high-resolution mobile laser scanning system, which can create 3D maps with a high density and high accuracy. We realized an accurate system calibration procedure and evaluated the system thoroughly, demonstrating a point to point accuracy of the resulting point cloud in the order of one centimetre. We also present an application example.

4.1 Measurement System

In mobile laser scanning, an object point $\mathbf{x}_o^s = [x_o^s, y_o^s, z_o^s]^T$ in the local sensor frame of the 2D laser scanner can be written as $[0, d_s \sin(b_s), d_s \cos(b_s)]^T$, where d_s is the measured distance and b_s the scanning angle. In order to obtain a georeferenced point cloud, the object points of the 2D laser scanner have to be transformed

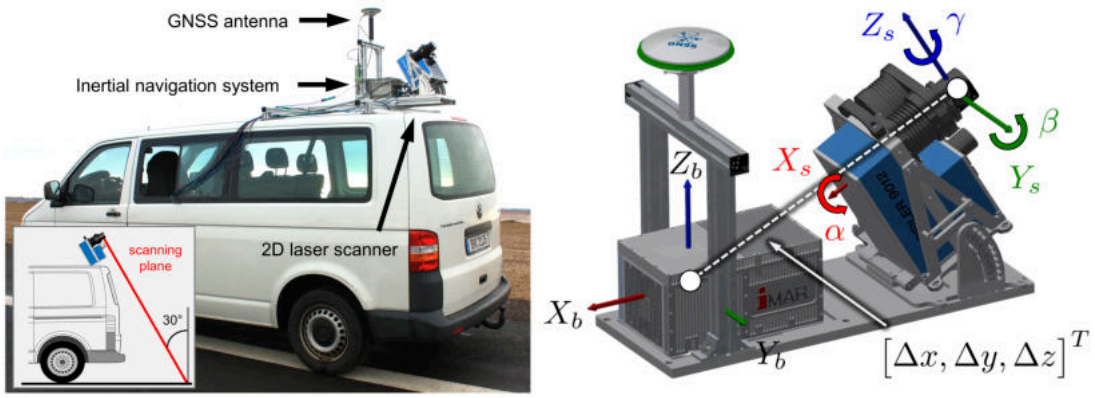

Figure 4.1: Mobile Mapping System mounted on a vehicle (left). Scanner and INS with system calibration parameters (right).

into the body-frame of the platform, which coincides with the coordinate system of the IMU. For this transformation, the extrinsic calibration parameters are needed, i. e., the lever arm $[\Delta x, \Delta y, \Delta z]^T$ as well as the boresight angles α, β, and γ (Fig. 4.1, left). Subsequently, the orientation angles of the platform, i. e., roll ϕ, pitch θ, and yaw ψ, and the translation vector $\boldsymbol{t}_b^g = [t_e, t_n, t_h]^T$ are used to transform the object points into the global coordinate system. All these transformations can be combined to the georeferencing equation, which provides georeferenced scan points $\mathbf{x}_o^g = [x_o^g, y_o^g, z_o^g]^T$:

$$\begin{bmatrix} x_o^g \\ y_o^g \\ z_o^g \end{bmatrix} = \begin{bmatrix} t_e \\ t_n \\ t_h \end{bmatrix} + \boldsymbol{R}_b^g(\phi, \theta, \psi) \left(\boldsymbol{R}_s^b(\alpha, \beta, \gamma) \begin{bmatrix} x_s \\ y_s \\ z_s \end{bmatrix} + \begin{bmatrix} \Delta x \\ \Delta y \\ \Delta z \end{bmatrix} \right). \tag{4.1}$$

Here we assume that the global coordinate system is a local level system aligned with the North and the gravity directions. This simplifies the georeferencing equation because the reference frame for the position and the rotation is the same, and we avoid an extra rotation between the navigation (n) and the Earth (e) frame (see Sec. 2.1). Please note that the trajectory parameters $\boldsymbol{R}_b^g(\phi, \theta, \psi)$ and $\boldsymbol{t}_b^g$ are needed for the exact moments, where the laser measurements $\mathbf{x}_o^s$ have been taken. This requires proper synchronization between the different sensor systems and potentially an interpolation of the poses between measurements. The determination of $[\Delta x, \Delta y, \Delta z]^T$ and $\boldsymbol{R}_s^b(\alpha, \beta, \gamma)$ is called system calibration and will be explained in the following.

4.2 System Calibration

In [J16], [C4] and [J7] we developed and evaluated a calibration procedure, which allows the determination of the lever arm $[\Delta x, \Delta y, \Delta z]^T$ and boresight angles (α, β, γ) between a profile laser scanner and the IMU coordinate system of the

platform. The latter represents the body frame in most sensor setups. The calibration procedure is based on a carefully designed plane setup, in which we move the system while it is recording laser scans and pose information. Using the pose, which is in this case estimated from GNSS and IMU readings, and initial values for the calibration parameters, we can georeference each scan profile as described in Eq. 4.1 (Fig. 4.2, right column). We estimate the calibration parameters in a least-square adjustment procedure by minimizing the distance between those profiles and the previously known plane parameters. We created the plane parameters from a TLS scan of the environment, which we georeferenced in the same coordinate system as the estimated poses (Fig. 4.2, left column). We

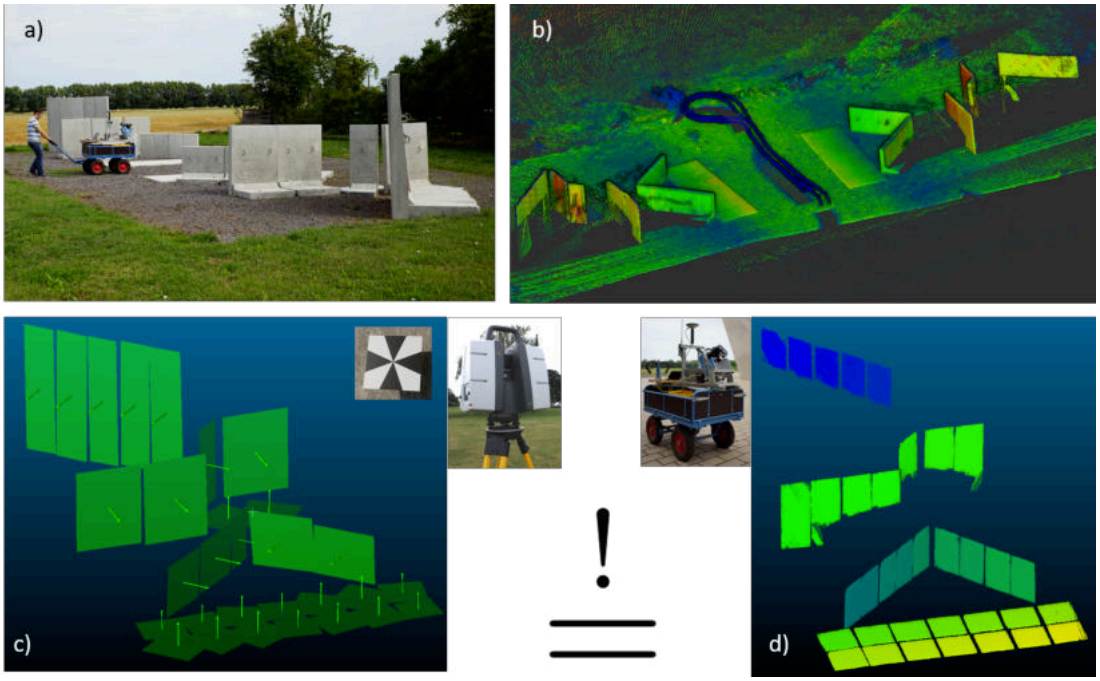

Figure 4.2: a) Plane setup consisting of concrete blocks. b) point cloud resulting from the system. c) planes extracted from TLS scan. d) planes extracted from mobile scan. [J7]

designed the arrangement of the planes so that the sensitivity of the measured profiles to the calibration parameters is high and that the influence of the pose estimation on the estimated parameters is low. For example, by driving through the symmetric setup in two directions, some systematic errors in the trajectory estimation are cancelled out or minimized. Repeating the procedure at different times also reduces the influence of systematic errors coming from the satellite constellation.

Experiment and analysis of the calibration results show that the empirical accuracy of parameters is in the order of millimetres for the lever arm and millidegrees for the boresight angles (Fig. 4.3). This leads to point errors of the resulting point clouds, which are below 1 mm up to distances of 50 m [J7]. We can conclude that the proposed procedure has an accuracy, which does not lead

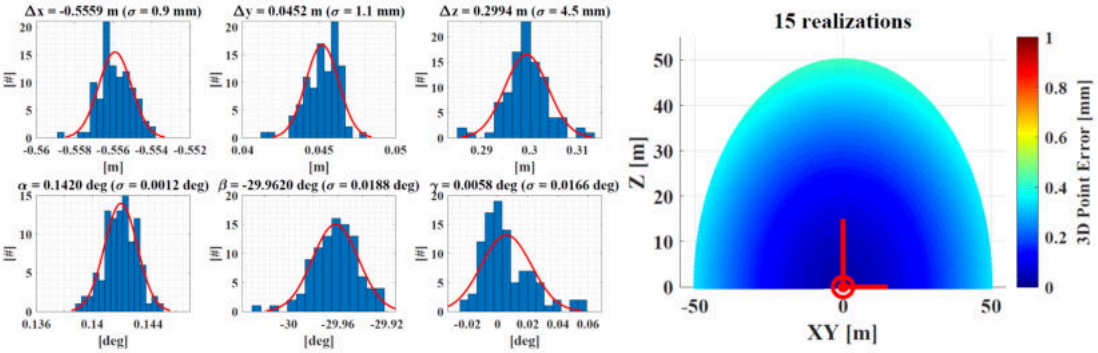

Figure 4.3: a) Distribution of calibration parameters for 100 calibration runs. b) Point error of the resulting point clouds for distances up to 50 m. Here 15 calibration runs have been performed and combined. [J7]

to higher errors than other expected errors coming from the laser scanner measurement itself or the trajectory estimation.

4.3 Quality Analysis

To determine the quality of the resulting point cloud, we set up an environment with several pillars and laser scanner targets. We determined their coordinates with an accuracy below one millimetre (Fig. 4.4). After driving through this environment, we extract the target coordinates from the resulting point cloud and compare them with their nominal coordinates [J7]. The results are visualized in Fig. 4.5. The distribution of the errors for the different coordinate axis shows

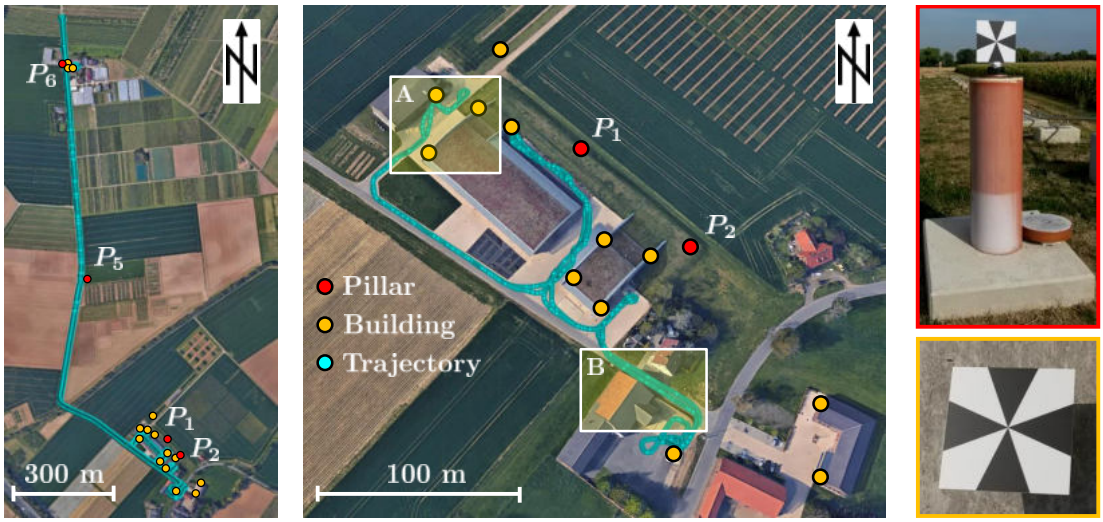

Figure 4.4: Test environment and trajectory (blue) of the mapping system. The pillars (red) and target (yellow) positions were used for evaluation.[J7]

no significant systematic effects as they may arise from calibration errors. The standard deviation is below one centimetre for all axis, which is in the order of

the expected accuracy of the position determination using a GNSS/IMU combination in an ideal environment. The quality assessment of point clouds resulting from a mobile laser scanning system is a challenging task. The reason is that the determination of all components of the transformation chain (Eq. 1.2) includes many uncertainties, for which the true distributions are often unknown. An empirical approach seems to be a suitable option to address this problem. However, the actual quality parameters of interest are unclear in advance and will depend strongly on the application. Addressing these issues is the subject of current research activities. Therefore, we only show here the empirical point error using scanner targets.

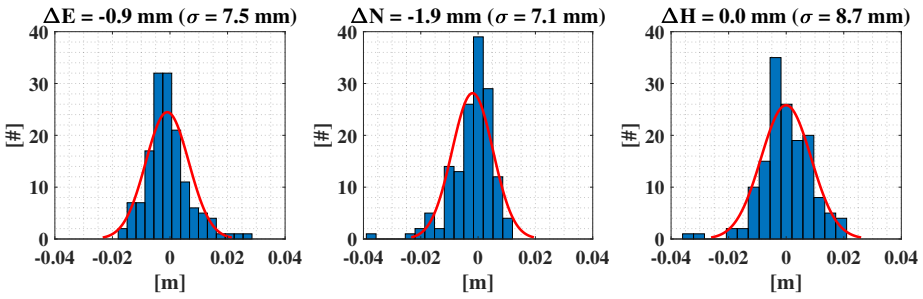

Figure 4.5: Point errors of detected targets, separated in North, East and Height directions [J7].

4.4 Application Example: Road Monitoring

One application where we used the system described above is the monitoring of a road surface [J10]. The main goal of the investigation was to see if it is possible to detect critical settlements of the road surfaces. Due to the lack of a second epoch with a known settlement, we compared the height values resulting from the mobile scan with reference height determined using a high precision levelling procedure. One of the challenges of this comparison was that the reference heights were determined with respect to the Geoid, while the heights from the mobile mapping system are relative to the ellipsoid. Therefore, the difference between both (*geoundulation*) and its change along the test track (Fig. 4.6b) has to be known and considered. Initially, we determined the geoundulation along the test track using levelling and GNSS measurements at different stations for the investigation. As described above, we then created a mobile scan of the test track, using the laser scanner targets on the road to mark the points of interest (Fig. 4.6c). We extracted the coordinates of the targets and corrected the height using the geoundulation and the target height and then compared it with the reference heights from the levelling. The results are shown in Fig. 4.6d. The standard deviation of the errors is below a centimetre, and therefore, potential

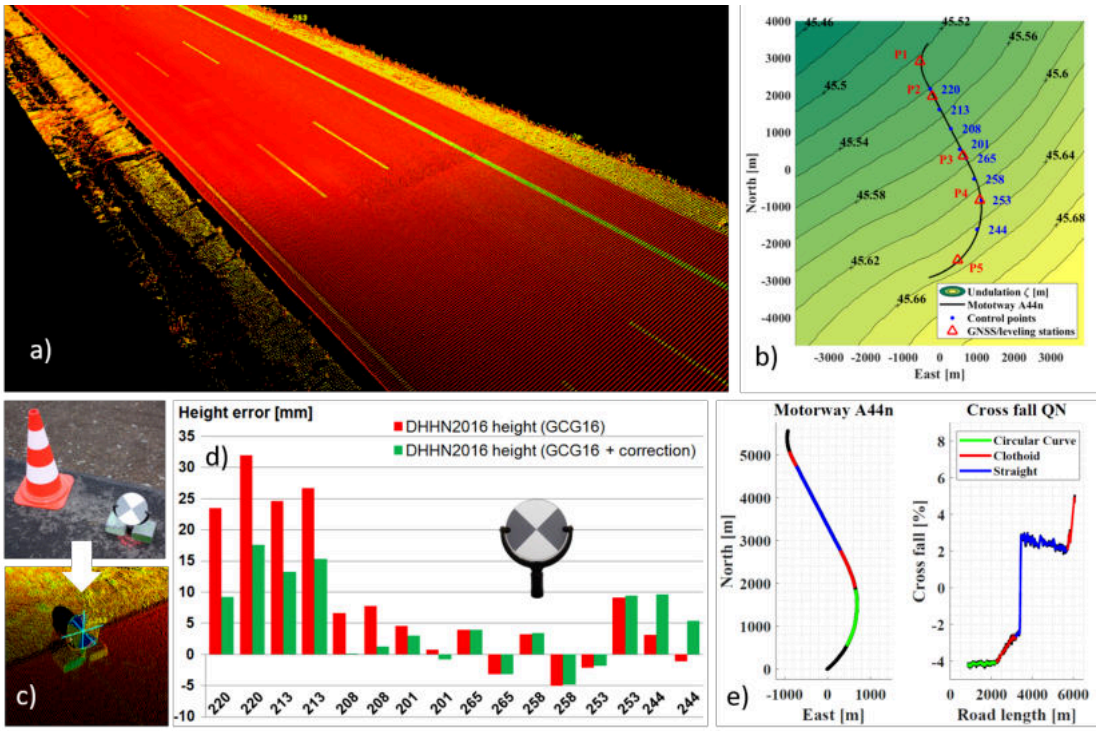

Figure 4.6: a) Mobile scan of a piece of the Highway. b) Geoundulation in the area of the test track. c) Targets, which have been used to evaluate the results. d) Resulting errors of height values along the test track. e) Cross fall extracted from the scan profiles.

settlements might be detected when they are bigger than several centimetres. Fig. 4.6e shows the measured cross fall of the road for the different parts of the test track. We calculated this parameter from the scan profiles and other road-related parameters, such as the rut depth or the fictive water depth.

Chapter 5

Mapping With UAVs

Unmanned Aerial Vehicles (UAVs) allow for mapping areas that are not easily accessible by ground-based vehicles. Depending on the sensor setup and the drone, it is also possible to map large areas within a short amount of time. A challenge of UAV-based mapping usually comes with the limited payload of the platform. High-resolution laser scanners and high-grade IMUs, as presented in the previous chapter, are too heavy, too large, and often to power-hungy to be carried by a UAV. This chapter presents systems which mostly use cameras as mapping sensors. We present various applications, such as deformation monitoring or agriculture, and describe how we created and georeferenced the maps and evaluated the results.

5.1 Mapping on Demand

[C10] **Klingbeil**, L., Nieuwenhuisen, M., Schneider, J., Eling, C., Droeschel, D., Holz, D., Läbe, T., Förstner, W., Behnke, S., and Kuhlmann, H. (**2014**b). Towards autonomous navigation of a UAV-based mobile mapping system. In *2014 International Conference on Machine Control and Guidance (MCG)*, pages 136–147

[J20] Eling, C., **Klingbeil**, L., Wieland, M., and Kuhlmann, H. (**2014**). Direct georeferencing of micro aerial vehicles - system design, system calibration and first evaluation tests. *Photogrammetrie - Fernerkundung - Geoinformation*, 2014(4):227–237

[J17] Eling, C., **Klingbeil**, L., and Kuhlmann, H. (**2015**a). Real-time single-frequency GPS / MEMS - IMU attitude determination of lightweight UAVs. *Sensors*, 15(10):26212–26235

[C9] Eling, C., Wieland, M., Hess, C., **Klingbeil**, L., and Kuhlmann, H. (**2015**b). Development and evaluation of a UAV-based mapping system for remote sensing and surveying applications. *The International Archives of the Photogrammetry, Remote Sensing and Spatial Information Sciences*, XL-1/W4(1W4):233–239

The goal of the DFG (Deutsche Forschungsgemeinschaft) funded research unit *Mapping on Demand* was to develop a lightweight, autonomously flying UAV that

can identify and measure inaccessible three-dimensional objects using visual information. A major challenge comes with the term on-demand. Apart from the classical mapping part, where 3D information is extracted from aerial images, the UAV was intended to fly fully autonomous based on a high-level user request. It should avoid obstacles and process mapping data in real-time, including extracting semantic information. Several project partners from different scientific disciplines, such as computer vision, robotics, geodesy, photogrammetry, geoinformation, and computer graphics, developed methods to reach the goal. We provide an overview of the research unit in [C10]. One task in reaching the

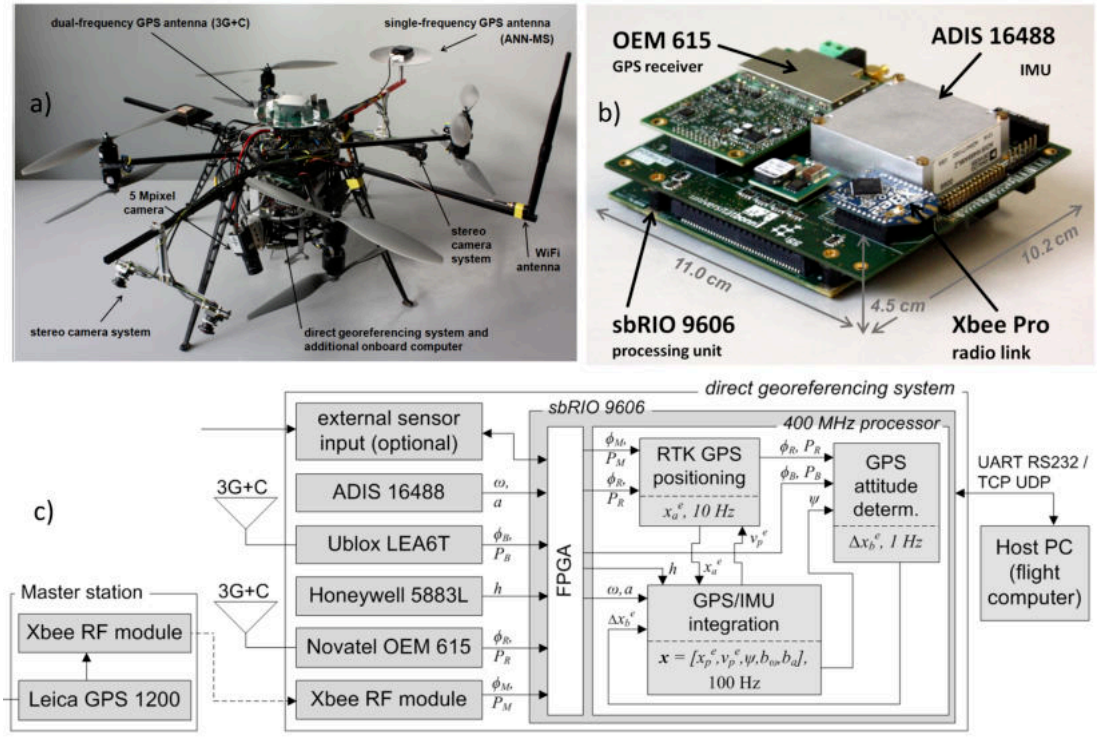

Figure 5.1: a) UAV platform, developed within the project. b) multi-sensor unit, developed for real-time trajectory estimation. c) Block diagram of the multi-sensor unit and sensor data flow.

project goals was determining the accurate position and orientation of the flying platform in real-time. This was necessary for several reasons. At first, precise pose estimation is necessary for the device's navigation. Suppose, a mission is planned based on previously generated map data or existing low-level building models. In that case, the vehicle's pose needs to be available in real-time in a global coordinate system. Also, precise pose estimation is needed to create georeferenced maps directly during the flight.

During the project, we developed a UAV, which contained two grey-scale stereo fish-eye camera pairs and a higher resolution RGB camera (Fig. 5.1). It also contained a sensor unit, which we specifically developed to provide accurate 3D position and orientation data in real-time. The sensor system contains a

dual-frequency GNSS receiver, a tactical grade Inertial Measurement Unit, and a magnetic field sensor. We used a second single-frequency GNSS receiver to create a short 1 m baseline between two antennas on the UAV to derive additional information about the heading of the platform. As described in Ch. 2 and detailed in [J20] and [J17], we fused these sensors using a Kalman Filter to provide a 6D pose estimation in real-time with an accuracy in the order of centimetres for the position and degrees for the orientation. With the development, we focused on the real-time capability in the two senses. One is that the sensor estimates the pose during motion, which implies the need for a radio module that constantly receives GNSS correction data from a nearby reference station. The other one is that the system is implemented on a real-time capable embedded computer, guaranteeing task completion within a specific time and enabling a very high synchronization accuracy for images and other sensors. We evaluated the accu-

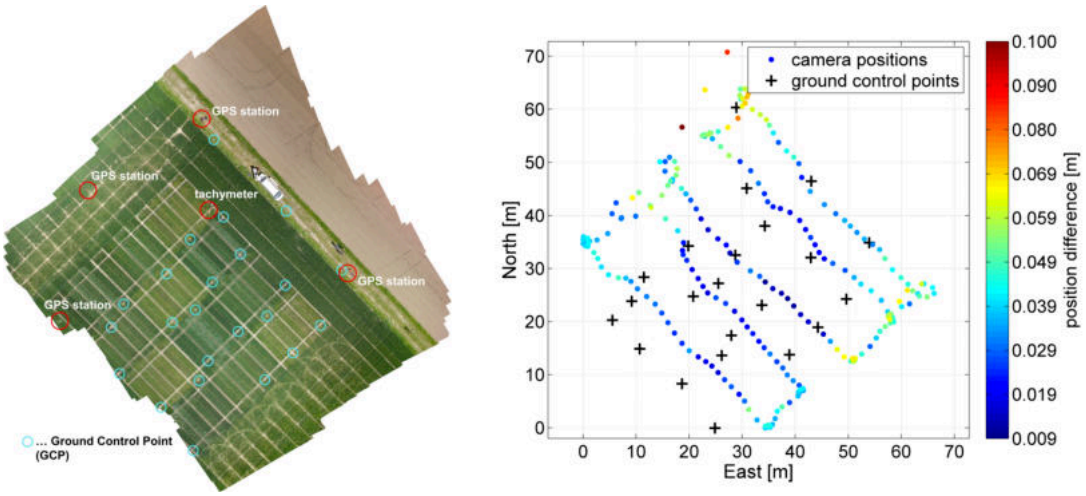

Figure 5.2: left) experimental setup used in the evaluation. right) camera positions and differences between on-board calculation and reference.

racy of the georeferencing unit described above by flying a UAV mission as it is usually performed to create an orthophoto of an area. During the mission, we recorded a few hundred overlapping images, and the georeferencing unit logged the current pose of the camera every time an image was captured. As a reference solution, we calculated the camera positions in a post-processing step using a bundle adjustment procedure, incorporating a set of ground control points with known coordinates. The differences are shown in Fig. 5.2 right, and it can be seen that they are mostly below 3 cm, which corresponds to the expected GNSS accuracy. The slightly higher deviations in the outer regions of the area a very likely caused by the bowl effect in the bundle adjustment and, therefore, inherent to the reference data.

5.2 Deformation Monitoring

[C8] Eling, C., **Klingbeil**, L., Wieland, M., and Kuhlmann, H. (**2016**). Towards deformation monitoring with UAV- based mobile mapping systems. In *2016 Joint International Symposium on Deformation Monitoring (JISDM), TU Wien, Vienna*

[J13] Eichel, J., Draebing, D., **Klingbeil**, L., Wieland, M., Eling, C., Schmidtlein, S., Kuhlmann, H., and Dikau, R. (**2017**). Solifluction meets vegetation: the role of biogeomorphic feedbacks for turf-banked solifluction lobe development. *Earth Surface Processes and Landforms*, 42(11):1623–1635

[C5] Holst, C., **Klingbeil**, L., Esser, F., and Kuhlmann, H. (**2017**). Using point cloud comparisons for revealing deformations of natural and artificial objects. In *2017 International Conference on Engineering Surveying (INGEO)*, pages 265–274

[C1] **Klingbeil**, L., Heinz, E., Wieland, M., Eichel, J., Laebe, T., and Kuhlmann, H. (**2019**). On the UAV-based analysis of slow geomorphological processes: A case study at a solifluction lobe in the turtmann valley. In *2019 Joint International Symposium on Deformation Monitoring (JISDM), Athens, Greece*

[J6] Eichel, J., Draebing, D., Kattenborn, T., Senn, J. A., **Klingbeil**, L., Wieland, M., and Heinz, E. (**2020**). Unmanned aerial vehicle-based mapping of turf-banked solifluction lobe movement and its relation to material , geomorphometric , thermal and vegetation properties. *Permafrost and Periglacial Processes*, 31(1):97–109

Deformation monitoring is the measurement of the geometric state of an object, e.g. the shape and the position, and the detection and analysis of the change of this state between several epochs. The objects might be natural, such as mountain slopes and glaciers, or artificial, like bridges and buildings. The deformations might be rigid, such as rotation and translation, or non-rigid, such as sheering or bending. Examples of deformation monitoring are observing sliding slopes to warn in risky situations or monitoring a water dam. Classically deformation monitoring has been realized using point measurements or geodetic networks with GNSS receivers and total stations. More and more area-based measurement methods, such as laser scanning, have been used recently. Those methods bring up new challenges in data analysis, such as the measurements being often irregular samples of the surface instead of dedicated and signalled observation points. Another level of complexity arises when the measurement platform is moving while it is performing the data capturing.

The accuracy of the measurements is crucial information to know in deformation monitoring, especially when it is in the same order of magnitude as the expected deformation. In kinematic measuring modes, this accuracy is significantly influenced by the accuracy of the trajectory estimation. In the case of image-based point clouds, the 3D processing procedure, including the structure-from-motion and the multi-view-stereo pipeline, also has a non-trivial impact on the resulting accuracy.

In the above papers, we investigated the usage of UAV imagery for deformation monitoring. In [C8] we placed several objects in an area of about $10\,\mathrm{x}10\,\mathrm{m}^2$.

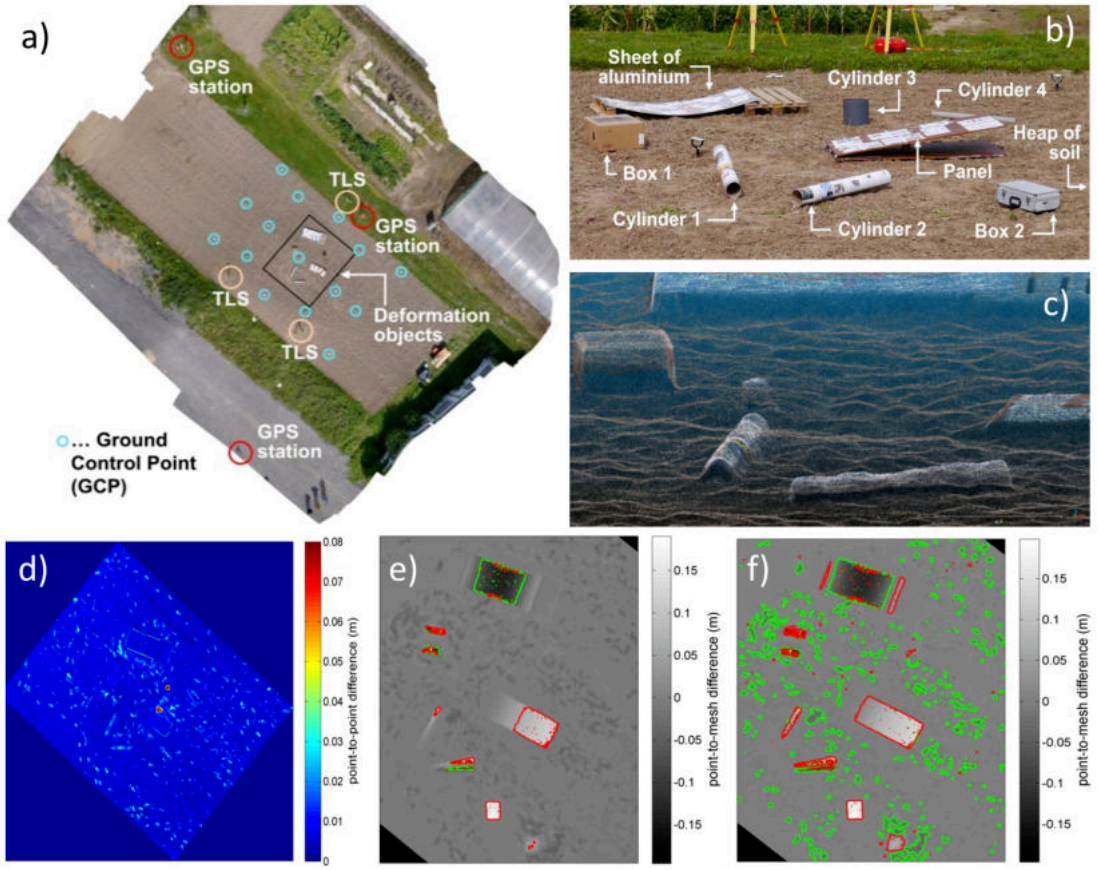

Figure 5.3: a) Test environment for deformation analysis trial. b) Closer view of the objects and c) measured point cloud from that area. d) Differences between the imaged based point cloud and the TLS scan. e) Detected deformations without fine-registration and f) with fine-registration.

We captured the scene as a point cloud using UAV images and a structure-from-motion / multi-view stereo processing pipeline (Fig. 5.3a-c). We performed the georeferencing by measuring the camera coordinates at the image capturing time without ground control points. We repeated this two times, and in between, we changed the objects by several rigid and non-rigid deformations. We also captured a reference point cloud using a terrestrial laser scanner at multiple standpoints and georeferenced it using scanner targets. Fig. 5.3d shows that the differences between the TLS and the image-based point clouds are within $1-2$ cm. Only the footsteps left in the sandy area by the person carrying the laser scanner are visible here as deviations to the reference. Fig. 5.3e and f show detected significant deformations for two different cases. In the first case, we registered the point clouds of the different epochs only based on the georeferencing results from the sensor unit. We applied an additional fine registration step using an Iterative Closest Point (ICP) algorithm in the second case. Expectedly, we detected more minor deformations with the second approach, such as the footsteps. Nevertheless, even without the ICP fine registration, we detected deformations from about 7 cm.

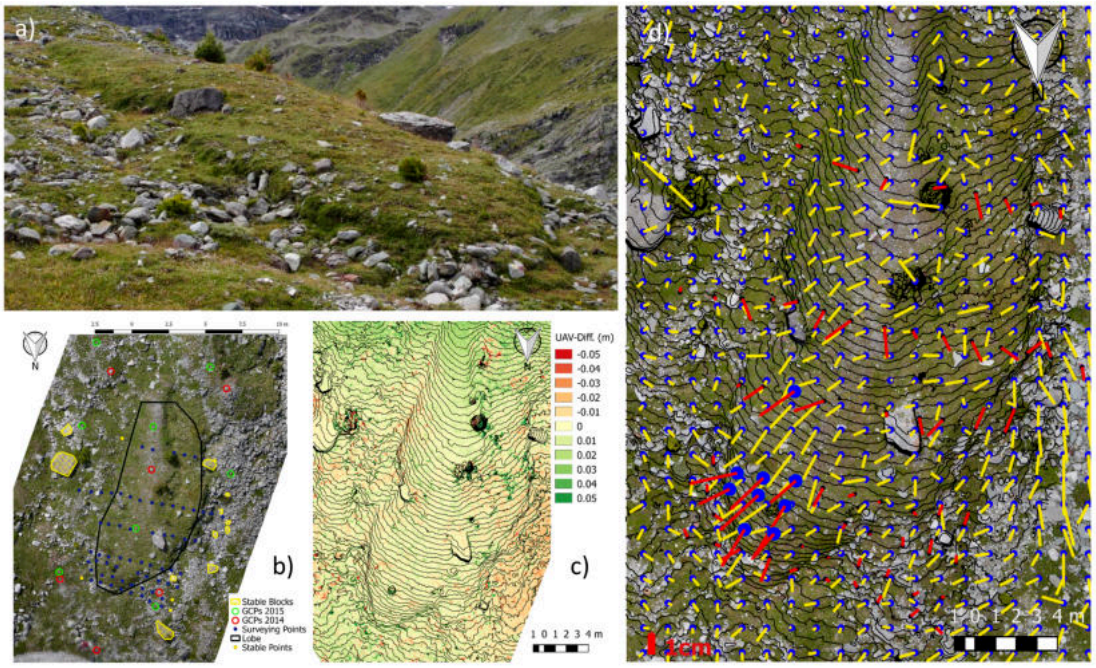

Figure 5.4: a) Solifluction lobe. b) Map of the environmemt including relevant objects and sensor positions. c) Difference between the epochs using point cloud comparison. d) Detected motion between the epochs using feature tracking and total station measurements.

In [J13], [C5], [C1], and [J6] we used a UAV equipped with a camera to study the movement properties of a solifluction lobe. These geomorphological objects move down a slope due to freeze-thaw processes. The expected movement is in the order of centimetres per year, and in [C1], we investigated if this movement can be detected using UAV images. We performed two flight campaigns in 2014 and 2015 in the Turtmann Valley in the Swiss Alps. We mapped an area with such a lobe (Fig. 5.4 a) using a UAV with a camera and a flight height of about 10 m. We processed the images to a georeferenced point cloud using the structure-from-motion pipeline in Agisoft Metashape and ground control points, which we measured using RTK. Since this registration only leads to an accuracy of up to a few centimetres, we applied a fine registration of the point clouds, using stable rocks around the area of interest as reference areas (Fig. 5.4 b).

A point cloud comparison between the two epochs (Fig. 5.4 c) showed no significant changes, apart from very local changes due to little rocks and stones and vegetation. We can explain this because the expected deformation is a motion along the surface, which might not be detectable using a direct point comparison. We proposed and tested an alternative option based on tracking automatically detected feature points in the orthophotos from both epochs. Fig. 5.4 d shows promising initial results of this procedure together with a reference, which we created with total station observations at distinct points on the lobe. We observed a motion of about 2 cm between the epochs at the front of the lobe with the total

station. The feature-based optical tracking showed results in the same order of magnitude and the same direction down the slope. A thorough investigation of this method was beyond the scope of the paper.

5.3 Agriculture

[C2] Becirevic, D., **Klingbeil**, L., Honecker, A., Schumann, H., Rascher, U., Léon, J., and Kuhlmann, H. (**2019**). On the derivation of crop heights from multitemporal UAV-based imagery. *ISPRS Annals of the Photogrammetry, Remote Sensing and Spatial Information Sciences*, IV-2/W5(2/W5):95–102

[J9] Wilke, N., Siegmann, B., **Klingbeil**, L., Burkart, A., Kraska, T., Muller, O., van Doorn, A., Heinemann, S., and Rascher, U. (**2019**). Quantifying lodging percentage and lodging severity using a UAV-based canopy height model combined with an objective threshold approach. *Remote Sensing*, 11(5):515

[J4] Honecker, A., Schumann, H., Becirevic, D., **Klingbeil**, L., Volland, K., Forberig, S., Jansen, M., Paulsen, H., Kuhlmann, H., and Léon, J. (**2020**). Plant, space and time - linked together in an integrative and scalable data management system for phenomic approaches in agronomic field trials. *Plant Methods*, 16(1):55

In the last section, we showed that changes along the surface of an object are difficult to detect using only 3D information, such as point clouds. If the direction of change is perpendicular to the surface, as in the case of growing vegetation, this is easier to achieve. In publications [C2], [J9], and [J4], we used point clouds generated from aerial images to monitor crop growth and to derive other agricultural parameters.

UAVs have become a widely used tool for monitoring vegetation, particularly in agricultural fields. The goal is often a fast and objective derivation of phenotypic parameters as they are needed in plant breeding trials or the monitoring of the general health status of the plants. The latter can control management actions, such as spraying or fertilizing. The UAVs are often equipped with multi- or hyperspectral sensors because the spectral reflectance can provide helpful information about the functional properties of plants. Our research focused on geometrical properties, which we derived from point clouds generated from images using the described structure-from-motion processing pipeline. In [C2], we generated georeferenced point clouds of winter wheat breeding trials at two locations in three seasons. From these data we generated *Crop Surface Models*, which are raster images containing the crop heights relative to the ground. We investigated different options for the rasterization of the point clouds and the generation of height values for each breeding plot. From the crop surface models of different dates, we derived crop height and growth curves for the different genotypes, seasons, locations and management systems. In [J9], we used the crops surface models to detect and quantify lodging area and severity. [J4] presents, how the derived parameters can be integrated into a data management system for field

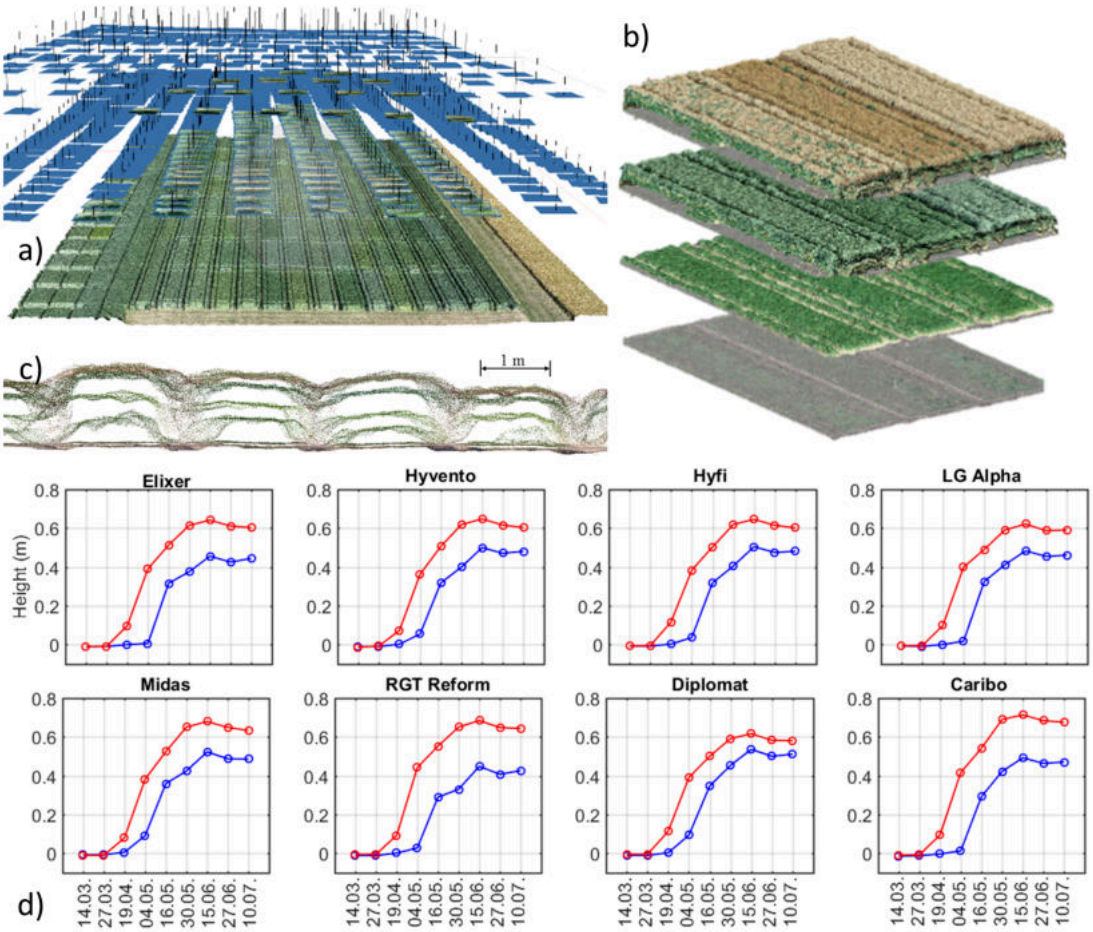

Figure 5.5: a) Winter wheat breeding trial and images taken during one mission. b) Generated point clouds for multiple epochs. c) Side view of point clouds from multiple epochs. d) Crop height development of several winter wheat genotypes for two different management systems: extensive (blue) and intensive (red).

trials and farmers.

5.4 UAV-Based Laser Scanning

[J2] Dreier, A., Janßen, J., Kuhlmann, H., and **Klingbeil**, L. (**2021**). Quality analysis of direct georeferencing in aspects of absolute accuracy and precision for a UAV-based laser scanning system. *Remote Sensing*, 13(18):3564

The above publications in the context of UAV mapping used cameras as sensors to create the 3D information. More and more laser scanners have been mounted on UAVs as mapping sensors in recent years. A shown in Fig. 5.6, the measurement principle is very similar to the one for mobile laser scanning presented in Ch. 4. A GNSS/IMU unit is used to determine the vehicle's trajectory, and with this, each scan profile is registered to the global reference frame. An

additional processing step is often applied to optimize the trajectory between the different flight strips.

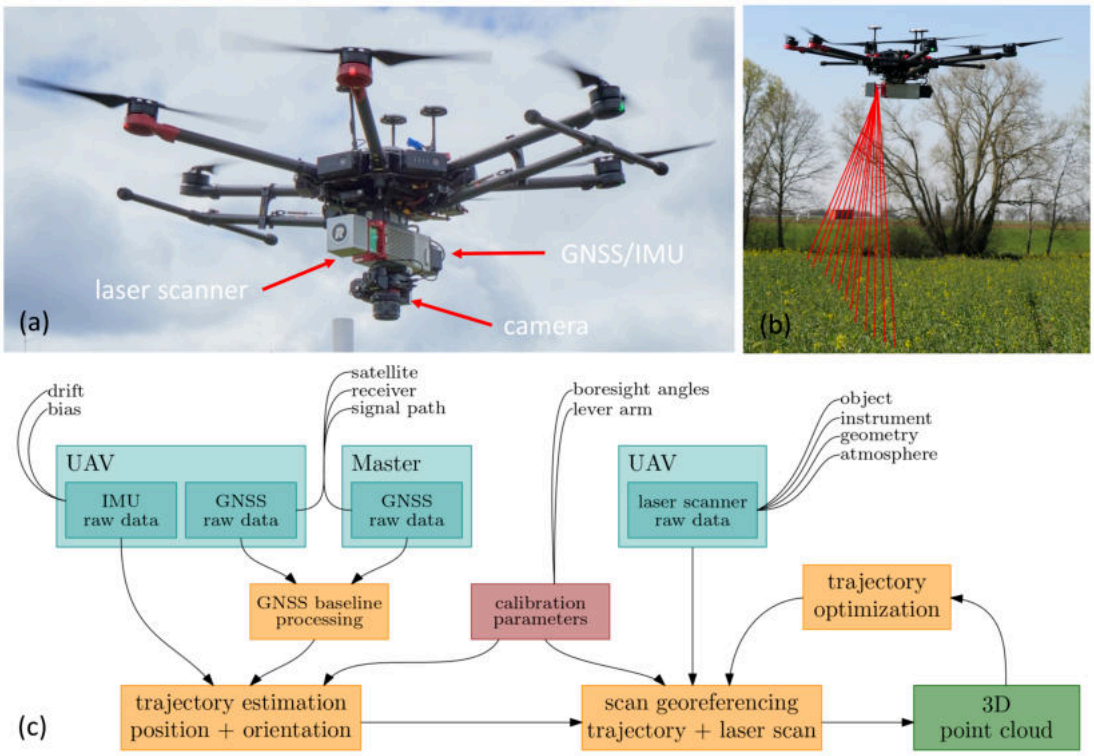

Figure 5.6: a) DJI Matrice 600 UAV with Riegl miniVUX-2UAV profile scanner. b) UAV scan profile. c) UAV laser scanning processing chain and main error sources.

In [J2], we empirically investigated the quality of a UAV laser scanning system with and without the additional optimization. We performed several test flights in two test environments to derive different quality parameters, such as the accuracy, the range precision and the impact of the GNSS base station. We showed that the point accuracy is in the order of a few centimetres for flight heights up to 25 m. The range precision for the same heights is below one centimetre. We also could not detect any influence of the source of the GNSS reference data (own master station versus RTK service) on the results. The applicability of UAV laser scanning to deformation analysis and crop monitoring are subjects of current investigations.

Chapter 6

High-Throughput Phenotyping in Viticulture

[J15] Rose, J. C., Kicherer, A., Wieland, M., **Klingbeil**, L., Töpfer, R., and Kuhlmann, H. (**2016**). Towards automated large-scale 3D phenotyping of vineyards under field conditions. *Sensors*, 16(12):2136

[J12] Kicherer, A., Herzog, K., Bendel, N., Klück, H. C., Backhaus, A., Wieland, M., Rose, J. C., **Klingbeil**, L., Läbe, T., Hohl, C., Petry, W., Kuhlmann, H., Seiffert, U., and Töpfer, R. (**2017**). Phenoliner: A new field phenotyping platform for grapevine research. *Sensors*, 17(7):1625

[C3] Zabawa, L., Kicherer, A., **Klingbeil**, L., Milioto, A., Töpfer, R., Kuhlmann, H., and Roscher, R. (**2019**). Detection of single grapevine berries in images using fully convolutional neural networks. In *2019 IEEE/CVF Conference on Computer Vision and Pattern Recognition Workshops (CVPRW)*, pages 2571–2579. IEEE

[J5] Zabawa, L., Kicherer, A., **Klingbeil**, L., Töpfer, R., Kuhlmann, H., and Roscher, R. (**2020**). Counting of grapevine berries in images via semantic segmentation using convolutional neural networks. *ISPRS Journal of Photogrammetry and Remote Sensing*, 164:73–83

[J1] Zabawa, L., Kicherer, A., **Klingbeil**, L., Töpfer, R., Roscher, R., and Kuhlmann, H. (**2022**). Image-based analysis of yield parameters in viticulture. *Biosystems Engineering*, 218:94–109

Yield estimation is of great interest in viticulture, since an early estimation could influence management decisions of winegrowers. The current practice involves destructive sampling of small sets in the field and a subsequent detailed analysis in the laboratory. The results are extrapolated to the field and only approximate the actual conditions. Within a series of publications, we developed methods to automatically count the number of berries and grapes in a vineyard using a mobile platform with multiple cameras.

6.1 Measurement System

We developed a mobile mapping platform based on a grapevine harvester with our project partners. The harvester can drive over the vine rows, building a

movable tunnel equipped with sensors. Within the tunnel, a multi-camera system consisting of four RGB and one infrared camera is mounted pointing from the side onto the canopy at about 70 cm. The tunnel allows controlling the lighting conditions, making the imaging procedure more reliable. The system also contains a GNSS receiver in RTK mode and a two-axis inclinometer. By combining the GNSS positions, the two angles, a motion model of the vehicle, and the relative transformations between all sensors, it was possible to georeference every picture taken with the cameras with an accuracy of a few centimetres. The system is presented in [J12] and shown in Fig. 6.1.

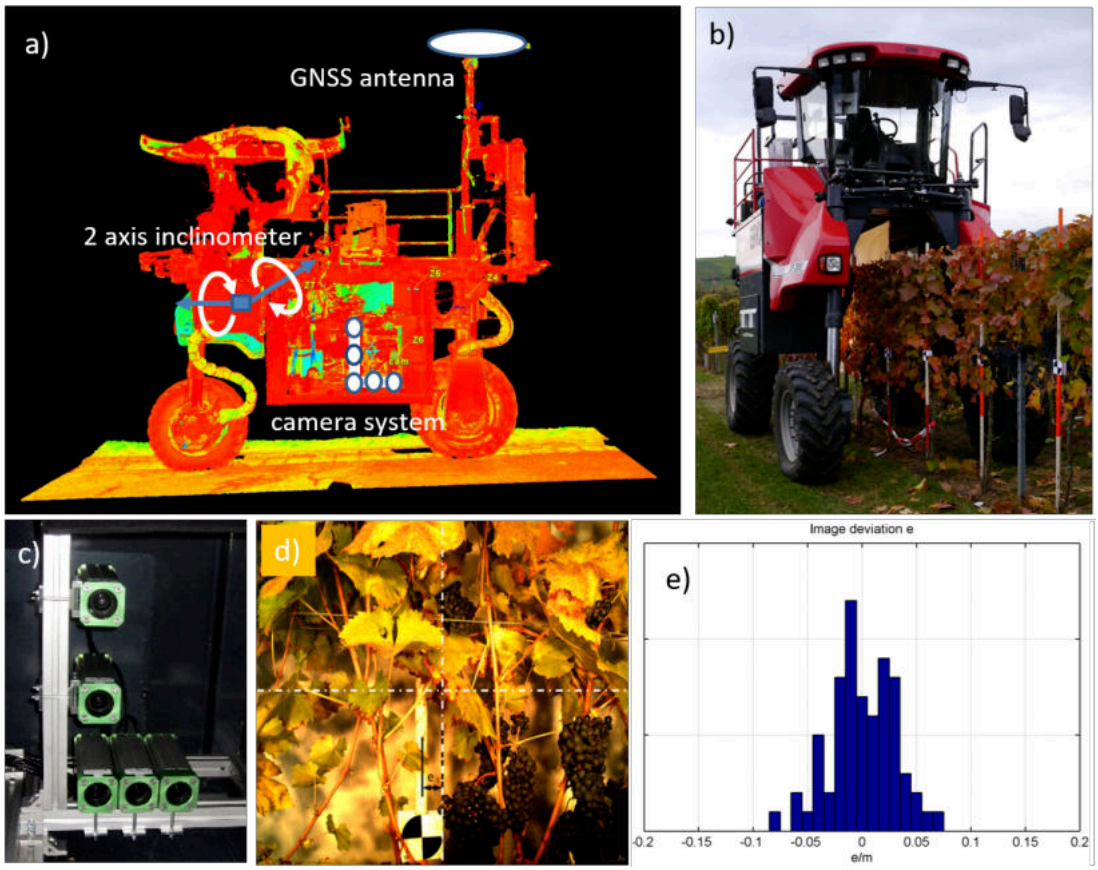

Figure 6.1: a) Modified grapevine harvester with additional sensors. b) Harvester driving over a vine row. c) Mult-camera system. d) Image taken in a vine row with one of the cameras. e) Deviation of detected camera coordinates from nominal positions.

6.2 Yield Estimation Using Point Clouds

To count the number of visible berries, we implemented a processing pipeline, which is based on point clouds [J15]. In a first step, we created the clouds from overlapping images taken with the multi-camera system while it was moving along the vine row. By integrating the accurate positions of the images, the

reconstruction process was stable and led to an adequately scaled and georeferenced reconstruction. After some preprocessing steps removing outliers, and subsampling the points, we separated berry and background points using a segmentation algorithm. The algorithm is based on an Import Vector Machine and several features exploiting the colour and the 3D structure of the neighbourhood of the points. We modelled each berry by fitting spheres into the segmented point clouds in the last step. We calculated the number and the size of the berries, the number of grape bunches, and the number of berries per bunch. We showed that the pipeline could detect between 70 and 90% of the visible berries. However, we also noticed that the performance depended on the quality of the 3D reconstruction from the images.

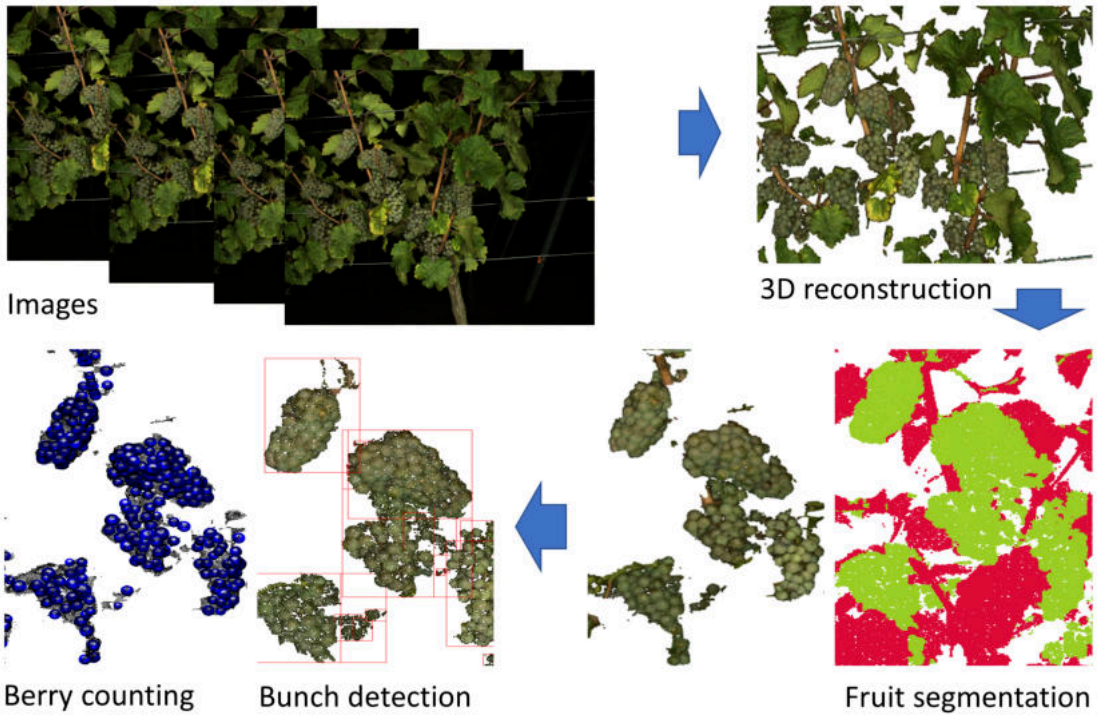

Figure 6.2: Pipeline from consecutive images taken with the mobile system to the 3D models of single berries, which are used to quantify the number and size of visible berries.

6.3 Image-Based Yield Estimation Using CNNs

The high computational burden of the 3D reconstruction, its influence on the segmentation, and at the same time, the increasing availability and demonstrated performance of Convolutional Neuronal Networks (CNN) for image understanding motivated the development of an alternative pipeline for yield estimation.

In [C3] and [J5], we presented a method to segment single berry instances in images to count them. While other instance segmentation algorithms had trouble

with a high number of instances in one image, we proposed an approach which transforms the problem into a simpler segmentation problem by classifying pixels into the three classes *berry*, *edge*, and *background*. The existence of an edge class spatially separates individual berries and makes them localizable and countable. The correlation between the number of detected berries and the number of manually counted berries in a set of 60 images was nearly 100%.

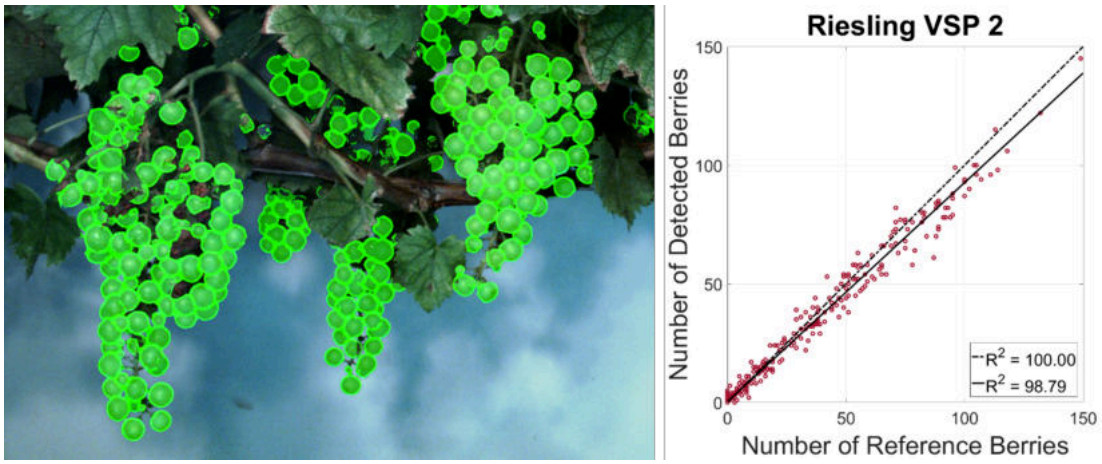

Figure 6.3: Left) Prediction of berries in an image. Right) Correlation between the true and the detected number of visible berries in 60 test images.

Although we showed that we could detect nearly all berries visible in the images, one critical question remains in the context of yield estimation: how many berries are not visible in the images? In [J1], we investigated how we can use the procedure above to estimate the yield in a vineyard. We analyzed data that we took with the mobile system in three different years from three different varieties. The vine has also been grown in two different training systems; one is the classical Vertical Shoot Positioned (VSP) system, and one is the Semi Minimal Pruned Hedge (SMPH) system. The latter has many branches and many leaves, leading to more occlusions. To analyze the effect of occlusion, we additionally performed an experiment where we captured data before and after removing the leaves. The reference yield for the different years and varieties in this experiment was provided in kg per row.

We first captured images as described above and counted the berries in each image. After that, we compensated for horizontal and vertical image overlap and double counting by utilizing the images' georeference and detecting counted grape bunches. To predict the yield, it was necessary to establish a relationship between the number of visible berries and the yield in kg. This relationship depends on the number of invisible berries and the berry weight. While the latter can be determined relatively quickly, the amount of invisible berries depends on the variety, the year, and the training system. The defoliation experiments showed

that in the SMPH system, the variability is so high that it is impossible to provide a helpful correction factor. In the VSP, we achieved a mean absolute yield prediction error of 26%, influenced mainly by the occlusion variability.

Chapter 7

Conclusion and Outlook

In this thesis, we presented methods for trajectory estimation of moving platforms and various examples of sensing systems and applications which use these methods to georeference data and generate maps. One part of our contributions was the field of sensors and methods for trajectory estimation in general. We developed system configurations, calibration procedures and algorithms, which mainly focussed on the integration of inertial sensors with other observations, e.g. from GNSS or magnetometers. The other part of our contribution focussed on particular application examples of mobile mapping for surveying, agriculture and deformation analysis.

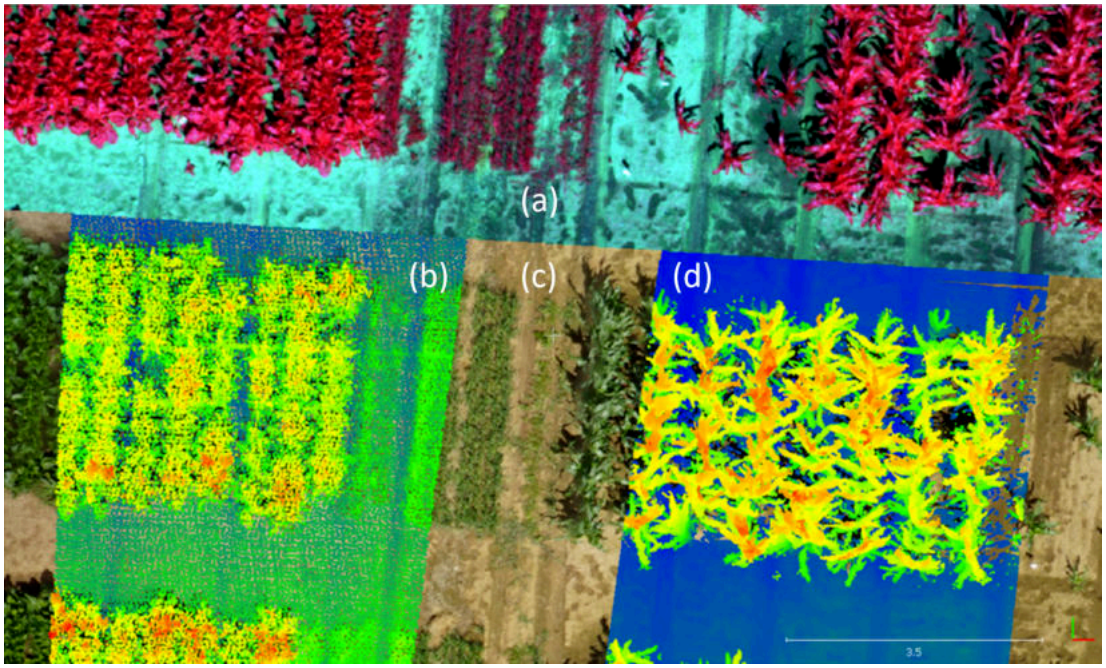

Figure 7.1: a) multispectral orthomosaic. b) UAV LIDAR point cloud, c) RGB orthomosaic. d) high-resolution mobile laser scanning point cloud.

Fig. 7.1 shows a segment of an agricultural field with an overlay of mapping

results from four different mobile mapping systems: an orthomosaic generated from multispectral images (a), a point cloud from a UAV-based laser scanner (b), an orthomosaic from RGB images (c), and a point cloud from a ground-based high-resolution mobile laser scanning system. We recorded, processed, and georeferenced the data as described in the examples in Chapters 4 and 5. We only created the overlay using the georeferencing information without any additional registration procedure. This image provides a qualitative insight into the accuracy of the presented mobile mapping systems and georeferencing methods. It also indicates the benefit, that the now possible intersection of these maps has in the agricultural context. Spatial data from different sources, can be combined to analyize, understand and predict crop health and growth, even on a single plant level.

Based on the publications that have been the basis for this thesis and all the experience gained throughout the years, we conclude with several remaining challenges and questions. We also present some ideas to answer the questions and to tackle those challenges.

GNSS Uncertainties GNSS receivers are very often the only sources of absolute position information, which enables registration to a global coordinate system. On the other hand, GNSS receivers are prone to systematic measurement errors, especially in urban environments or other areas with a disturbed line of sight to the satellites. The questions are whether these GNSS errors can be detected and corrected and if other sensors can sufficiently bridge and stabilize the trajectory estimation in those disturbed areas.

Low-Cost Sensors In order to derive centimetre or even better accuracy of the mapping products, the involved sensors are very costly. The interesting question is if we can achieve results with similar quality with low-cost sensors. This would enable the deployment of more platforms and increase the mapping process's efficiency even more.

Quality Analysis Depending on the application, reliable information about the quality of the resulting map products is essential. An open question is how to derive this information, given the complex chain of sensors and algorithms involved in generating the map.

A possible solution to adress GNSS uncertainties and enable low-cost systems is the integration of many sensing modalities and prior knowledge into the trajectory estimation procedure. The usage of images and laser scans can pro-

vide information about the relative motion of the platform and potentially avoid the need for expensive high-grade IMUs. While these methods have been widely used in the robotics community, they often generate local maps without a georeference. A combination of LIDAR, images, RTK GNSS and Inertial sensors, considering uncertainties of the sensors and algorithms involved, might provide georeferenced maps of high accuracy, even with low-cost sensors. Regarding the quality of results, relevant parameters need to be defined, and methods to derive those parameters need to be developed.